Flexible Printed RFID Sensor for Remote Potassium Ion Sensing

Tianhang Wu

Department of Electrical and Computer Engineering
Faculty of Engineering, McGill University
Montreal, Canada

August 2021

A thesis submitted to McGill University in partial fulfillment of the requirements for the degree of Master of Electrical Engineering

Acknowledgments

I would like to express my deep sense of gratitude to my supervisor - Prof. Sharmistha Bhadra and McGill University. Prof.Bhadra is a brilliant, patient, and interactive supervisor. I really thank her for providing me the opportunity to contribute to this research. I also would like to appreciate the assistance of my colleagues. Finally, I would like to thank my family especially my parents for their love and support.

Abstract

Potassium ion (K^+), one of the most common and abundant minerals, exists widely in plants, tissue of animals, extracellular spaces, and biological fluids. It is of great importance for the control and regulation of body functions in living organisms. Abnormal levels of potassium ions may result in a variety of pathological disorders. As the out of range potassium ions are seriously harmful, people need to control daily potassium intake. Therefore, an adequate amount of potassium needs to be present in foods and drinking water. A simple and cost-effective K^+ detection technique is preferred for monitoring levels of K^+ in food and drinking water packages/samples.

This thesis presents a flexible wireless passive printed RFID sensor based on a printed inductive-capacitive (LC) resonator circuit and a potassium ion-sensitive electrode (ISE) for remote potassium ion sensing. The potassium ion concentration of the contact solution could be wirelessly monitored by measuring the change of the RFID sensor's resonant frequency. The RFID sensor's resonant frequency can be directly detected by measuring the induced change in reflection coefficient (S11) of an external interrogator coil that is inductively coupled to the inductor of the RFID sensor. Results obtained for the RFID tag exhibit a second-order exponential relationship between the resonant frequency of the sensor and the K^+ concentration of the solution over 0.001-2 mole/L dynamic range values. Effects of varying separation distance and long-term monitoring on the sensor's performance are shown. The response time of the RFID tag is less than 1 second. The prototype RFID sensor has great market potential for low cost remote K^+ monitoring applications.

Abrégé

L'ion potassium (K^+), l'un des minéraux les plus communs et les plus abondants, existe largement dans les plantes, les tissus des animaux, les espaces extracellulaires et les fluides biologiques. Il est d'une grande importance pour le contrôle et la régulation des fonctions corporelles dans les organismes vivants. Des niveaux anormaux d'ions potassium peuvent entraîner une variété de troubles pathologiques. Comme les ions potassium hors de portée sont gravement nocifs, les gens doivent contrôler leur apport quotidien en potassium. Par conséquent, une quantité adéquate de potassium doit être présente dans les aliments et l'eau potable. Une technique de détection de K^+ simple et économique est préférable pour surveiller les niveaux de K^+ dans les emballages/échantillons d'aliments et d'eau potable.

Cette thèse présente un capteur RFID imprimé passif sans fil flexible basé sur un circuit résonateur inductif-capacitif (LC) imprimé et une électrode sélective d'ions potassium (ISE) pour la détection à distance d'ions potassium. La concentration en ions potassium de la solution de contact pourrait être surveillée sans fil en mesurant le changement de la fréquence de résonance du capteur RFID. La fréquence de résonance du capteur RFID peut être directement détectée en mesurant le changement induit du coefficient de réflexion (S11) d'une bobine interrogatrice externe qui est couplée par induction à l'inducteur du capteur RFID. Les résultats obtenus pour l'étiquette RFID présentent une relation exponentielle de second ordre entre la fréquence de résonance du capteur et la concentration K^+ de la solution sur des valeurs de plage dynamique de 0,001-2 mole/L. Les effets de la distance de séparation variable et de la surveillance à long terme sur les performances du capteur sont indiqués. Le temps de réponse de l'étiquette RFID est inférieur à 1 seconde. Le prototype de capteur RFID a un grand potentiel de marché pour les applications de surveillance à distance K^+ à faible coût.

Contents

List of Figures

List of Tables

Chapter 1

Introduction and Literature Review

1.1 Potassium Ion Sensing

Potassium ion (K^+), one of the most common and abundant minerals, exists widely in plants, tissue of animals, extracellular spaces, and biological fluids [1]. It is of great importance for the control and regulation of body functions in living organisms. It takes part in many vital biological processes, such as heartbeat regulation, nerve signal transmission, smooth muscle contraction, and kidney function [2, 3, 4]. It is important to maintain a consistent level of potassium in the blood and cells for normal bodily function. The normal plasma levels for potassium in adults range from 3.5 to 5.0 mEq/L. Abnormal levels of potassium ions may result in a variety of pathological disorders [5]. Too much potassium, called hyperkalemia, would lead to irritability, nausea, decreased urine production, and cardiac arrest [6]. On the other hand, with severe potassium deficiency, serious muscle weakness, bone fragility, central nervous system changes, decreased heart rate, and even death would happen [6].

One of the most essential roles for potassium ions in the human body is to control blood pressure (BP). High blood pressure, also known as hypertension, is one of the leading causes of cardiovascular disease (CVD) which affects approximately 1 billion individuals worldwide

[7]. More than 72 million Americans, nearly 1 in 3 adults, are estimated to have hypertension and nearly 70 million more adults are at risk of developing prehypertension [8, 9, 10, 11]. More than 90% of adults in the United States will probably develop hypertension, especially systolic elevations, by age 65 [9]. If no proper BP control is applied, hypertension significantly increases the risk of mortality and morbidity from CVD diseases such as stroke, coronary heart disease, congestive heart failure, and end-stage renal disease [7]. It not only harms the quality of patients' life but also puts a heavy financial burden on the social health care system. Hypertension remains the most common reason for patient visits to physician's offices. It is the primary reason for the use of prescription antihypertensive drugs, leading to an annual cost of almost $20 billion worldwide [12].

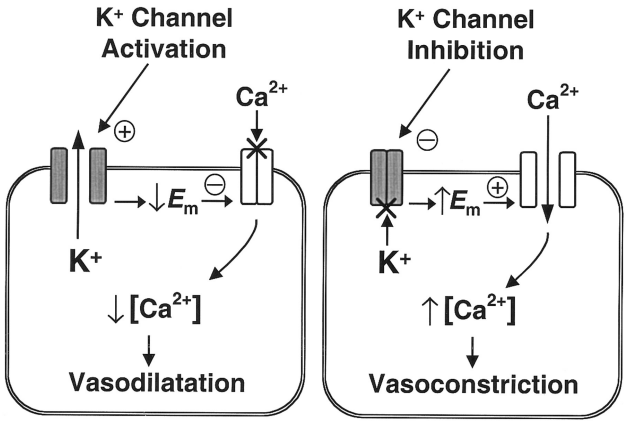

Figure 1.1 Schematic illustration of the key events involved in the vascular smooth muscle response to K^+ channel activation (left) or inhibition (right). Reprinted with permission from [13] © 2001, Wolters Kluwer Health

Hypertension cannot be easily cured since no vaccine is developed to prevent the development of high BP, but, its incidence can be decreased by reducing the risk factors for its development. Recent studies produced by Mark [12] suggested that dietary potassium intake could significantly lower BP in a dose-responsive manner. A diet rich in potassium promotes vasodilatation due to the potassium ion (K^+) channel opens in the vascular smooth muscle cell membrane while potassium depletion inhibits vasodilatation in contrast as shown in Figure 1.1 [13]. Other mechanisms by which potassium can influence BP include natriure-

sis, alterations in intracellular sodium and tonicity, modulation of baroreceptor sensitivity, reduced vasoconstrictive sensitivity to norepinephrine and angiotensin II, increased serum and urinary kallikrein, increased sodium/potassium ATPase activity and alteration in DNA synthesis and proliferation in vascular smooth muscle and sympathetic nervous system cells, improved insulin sensitivity, reduction in cardiac diastolic dysfunction, decrease in vascular neointimal formation, reduction in transforming growth factor (TGF)-β, and decreases in NADPH oxidase, oxidative stress, and inflammation [14, 15, 16, 17]. As a result, Mark [13] found that a high intake of potassium is important for the prevention of hypertension and major public health problems like CVA. As long as increasing the potassium intake to 4.7 g/day, the population systolic blood pressure (SBP) distributions would shift down by 1.7 to 3.2 mm Hg [12]. As predicted by Van Mierlo et. al [18], this small reduction in BP through increased dietary potassium intake on a population level would have a substantial impact in reducing CVD mortality with an estimated rate of 8% to 15%.

As the out-of-range potassium ions are seriously harmful, people need to control daily potassium intake. Therefore, an adequate but not excessive amount of potassium needs to be present in foods and drinking water. It is recommended to take 2000–4000 mg of potassium in the daily diet for healthy adults. The patients who suffer from hypertension are suggested to have a potassium intake of 4700 mg per day as mentioned above. Many processed food contains a lower level of potassium. Moreover, it is important to maintain a normal level of potassium in drinking water. Therefore, monitoring levels of potassium ions in food and drinking water packages/samples is of great importance for people's health and it has great market potential in the future.

1.2 Overview of RFID technology

The idea of Radio Frequency Identification (RFID) was first introduced in the early 20th century thanks to the development of radio broadcast technology during the Second World

War. The Identification Friend or Foe (IFF) system based on the same principle of RFID was created to identify allied planes [19]. Later in 1948, Harry Stockman [20] published a landmark paper "Communication by Means of Reflected Power" for the exploration of RFID. He foresaw the great potential of RFID based on reflected-power communication for its outstanding characteristics like high directivity, elimination of interference fading, and increased security [20]. Considerable research and development work in RFID has been done in the next couple of years after Stockman's publishment. Almost thirty years later Stockman's vision would reach fruition. The invention of the integrated circuit and microprocessors made possible the manufacturing of RFID with small size and affordable prices [19]. Nowadays, RFID is used for many applications such as animal tracking, goods dispensation, traffic management, etc.

An RFID system is usually composed of three main components: tag, reader, and server. The tag contains a built-in antenna to send and receive wireless signals and a chipset to save data. Each tag has a unique identifier code for distinguishability. The reader, also known as the interrogator, uses electromagnetic waves to collect information from the tags and transfer the signal to the processing unit. The server analyzes the information collected by the reader and provides the result. The basic working principle of an RFID system is: the reader gives out a certain frequency modulation signal containing information through the antenna; when the tag enters the active zone of the reader, its antenna will generate induction current through coupling, thereby giving corresponding energy to the electronic tag [21]. The induction current will activate the chipset circuit and the tag shall respond to reader according to the information received. Before transmitting the information stored in the chipset, the tag normally modulates the signal using phase or amplitude modulation on a predefined frequency carrier [19]. After the reader receives the signl sent by the RFID tag, it can identify the data inside the tag through demodulation and decoding and then redirect the data to the server for further processing.

The RFID systems can be classified into different types based on different criteria. According to tag's readable and rewritable nature, it can be divided to read-only tag and read-write tag; According to the talking order of tag and reader, it can be divided into RTF (Reader Talk First) and TTF (Tag Talk First); According to the different wavebands, it can be divided into low-frequency, high-frequency, ultrahigh-frequency and microwave tag [21]. Depending on the power source, the tag can be divided into passive, active, and semi-active tags. In general, operating frequency and power source are the main criteria for commercial RFID tags.

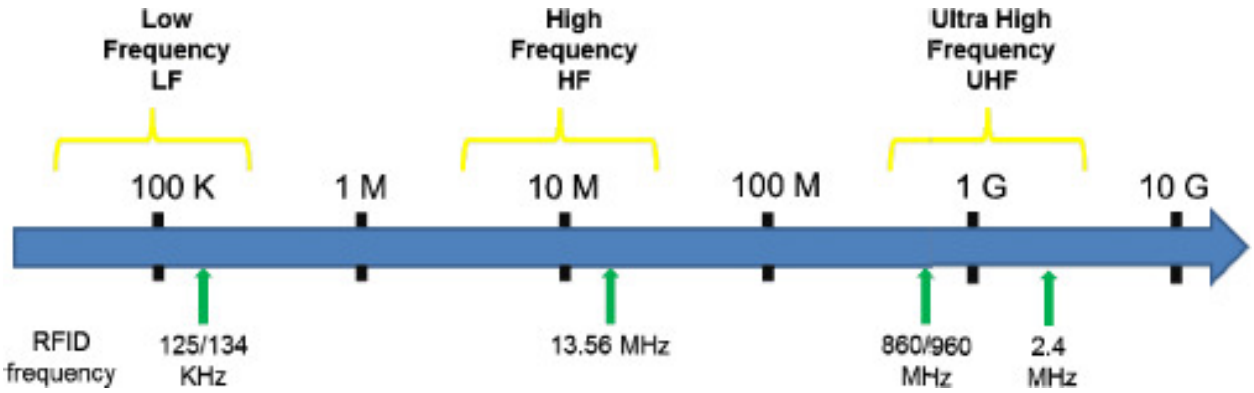

Figure 1.2 RFID frequency allocation. Reprinted with permission from [19] © 2011, IEEE

As mentioned, operating frequency is one of main factors in RFID. The performance of RFID systems working at different frequency bands differs from each other massively. Thus, the applications of RFID technology are related to the choice of operating frequency straightly. Figure 1.2 shows the frequency allocation of the RFID system.

1.2.1 Low Frequency RFID

Working bands for low frequency (LF) RFID systems are 30kHz - 300 kHz. The most common carriers used by the LF RFID system are 125 kHz and 134.2 kHz [19]. LF RFID tag is normally passive and has a short read range, usually within a few centimeters. LF waves can penetrate RF lucent material like water and thin metals [22]. They can also

operate in environments with high water content. Therefore, LF RFID systems are useful for applications requiring close range reading through high water content like animal identification and metal equipment such as vehicle immobilizers. The main drawback of the LF RFID is its low data transfer rate and poor anti-noise ability. For example, it is sensitive to electrical noise from the engines. This limits its application for simultaneous reading of multiple transponders in the industry [22].

1.2.2 High Frequency RFID

High frequency (HF) RFID tags operate at the frequency band of 3 MHz - 30 MHz. 13.56 MHz is the working frequency commonly used for HF RFID around the world. HF waves operate more like light waves, greatly reducing their effects near metals and liquids, and limiting their ability to penetrate materials [22]. Similar to the LF RFID tag, the HF RFID tag is usually passive and its effective operating range is within 50 cm. The activation energy is also obtained from the near field of the reader coupling inductor through inductive coupling. Compared to the LF RFID, the HF RFID has the advantage of lower costs due to the smaller antenna and better communication speed. It has been widely used in e-ticket, credit cards, electronic article surveillance (EAS), etc [21]. Due to the relatively low carrier frequency, both LF and HF RFID tags belong to near-field coupling tags that require an antenna coil. Figure 1.3 shows different types of near-field (LF and HF) tags such as nail tag, glass tag, disk tag, etc. One common problem for both LF and RF RFID tags is the limitation of operating distance. Since the power of the magnetic field of a magnetic dipole loop drops as $\frac{1}{r^6}$ in the near-field region, where r is the distance between a reader and a tag [23].

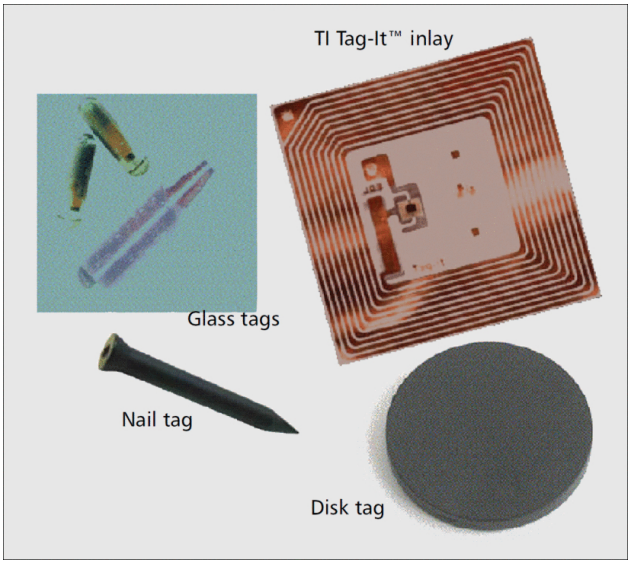

Figure 1.3 Sample near-field RFID tags (LF and HF). Reprinted with permission from [23] © 2007, IEEE

1.2.3 Ultrahigh Frequency RFID

The ultrahigh frequency (UHF) systems operate in the 300 MHz - 3 GHz range. The current RFID standard allows for multiple UHF spectrums worldwide. For example, the UHF range in the US is 902 MHz - 928 MHz while in Europe it is 866 MHz – 868 MHz [22]. UHF RFID tag operates at such an ultra-high frequency band that demands a small antenna, and it belongs to the far-field system. Differ from near-field tags, UHF RFID tags can be either passive or active. Figure 1.4 shows various form factors and antenna shapes used for UHF RFID tags to meet application requirements. Noted that reader antennas used for UHF RFID systems are usually directional antennas; the UHF RFID tags within the range of directional beams of the reader antenna can be read/written [22]. During work, UHF RFID tag will reflect the incoming signal from the reader after modulating it. This technique is called backscattering and adopted instead of induction [19].

The reading distance of UHF RFID system is limited by many factors as tag characteristics, propagation environment, and RFID reader parameters [24]. It is generally greater than 1m, usually 4 m - 6 m. The UHF system also allows identifying a bigger number of

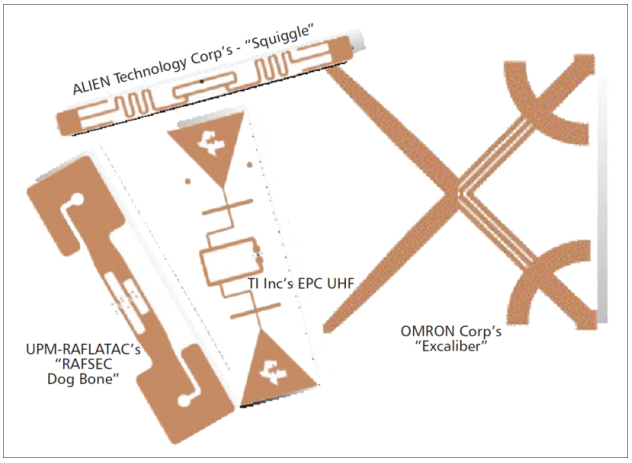

Figure 1.4 Various shapes of UHF tags. Reprinted with permission from [23] © 2007, IEEE

tags simultaneously thanks to its bit broadcasting protocol used for the anti-collision purpose. It is normally used in the retail chain and supply chain in the industry. However, the performance of UHF RFID tag degrades noticeably when it is near metal since the UHF waves can be easily reflected by metals [25].

The following table outlines the characteristics of LF, HF, and UHF systems.

Table 1.1 Characteristics of LF, HF, and UHF RFID systems.

Type	LF	HF	UHF
Reading range	A few centimeters	$\leq 50cm$	$\leq 50cm$
Pros	Not affected by high water content and thin metals	Low cost, Fast communication Speed	Long reading range, Multiple tags reading simultaneously
Cons	Low data rate, Noise	Less efficient for water and metals	Poor near metal performance
Application	Animal identification, Vehicle immobilizer	E-ticket, credit card	Retail chain, Supply chain

Apart from operating frequency, the power source is another main factor in RFID. Since the power source affects the manufacturing cost of the RFID tag as well as the long-term monitoring expense. Depending on the type of power source, the RFID tags could be divided into passive, active, and semi-active tags as follows.

1.2.4 Passive RFID

A passive RFID tag has no internal power source but it uses the electromagnetic (EM) field transmitted by a reader to power its internal circuit and send the response back [23]. Since it does not require an internal power source, the passive RFID tag is the least complex and usually the cheapest. It is suitable for mass production and long-term monitoring. But, the energy received from the reader is constrained and thus limits both the reading range and computing capacity of the chipset circuit. Without an onboard battery, it cannot store much information either.

1.2.5 Active RFID

The active RFID tag uses an inbuilt battery to activate the internal circuit and transmit the signal response. Due to the stable and strong internal power source, it can communicate over a much longer distance. The communication range of the active RFID is from several meters to tens of meters, i.e., up to 1000 m [26]. With the advancement of large-scale RF integrated circuits, the reading range of the active RFID will continue growing in the coming years. More sensors and memory could be installed on the tag's circuit and the active tag could provide more advanced features. However, due to usage of the internal battery, the fabrication cost of an active tag is much more expensive and the replacement of the dead battery costs more in the long term.

1.2.6 Semi-Active RFID

A semi-active tag uses an inbuilt battery to power up the internal circuit to realize the signal processing but it does not have an active transmitter. It still draws energy from the reader signal through inductive or radiative coupling to communicate with the reader. Compared with the passive RFID tag, its reading range is not limited by the short power range but the long communication range defined by operating frequency. It can support

more sensors and memory than a passive counterpart because of its onboard battery and is certainly cheaper than active tags. Similar to the active RFID tag, the major drawback of semi-active RFID tags is their limited lifespan issues due to the need for batteries to power up the tag circuitry. Once the batteries died, the tags cannot be used and the information stored in the memory of the tag chip could not be read [27]. As a consequence, ongoing maintenance is needed as the batteries have to be replaced.

In short, an overview of RFID technology is demonstrated. The RFID systems are classified with two main factors: operating frequency and power source. The advantages, drawbacks, and applications for each type of RFID are mentioned.

1.3 Ion sensitive electrode

Ion sensitive electrodes (ISEs) are common and cost-effective electrochemical sensors utilizing the principle of potentiometry for specific ion sensing. ISEs have great commercial potential due to their small size and portability, and low cost. They have been used in various areas, including clinical diagnostics, environmental monitoring, industrial process analysis, and agriculture [28, 29]. Figure 1.5 demonstrates a typical ISE for pH measurement consisting of a pH-sensitive measurement glass electrode and a separate reference electrode in a potassium chloride (KCl) gel-conducting solution. When the electrode is placed in an aqueous solution of unknown pH, the activity of the H^+ ions in the test solution is likely to be different from the activity of the H^+ ions in the hydrated layer, which sets up a potential difference between the solution and the surface of the membrane [30]. The law of electrochemical thermodynamics, also known as the Nernst equation, determines the potential difference between the membrane surface and the reference electrode. Based on the change of potential difference, the pH in the test solution can be calculated as the potential difference is linearly dependent on the logarithm of the activity of the H^+ ions.

In recent years, coated-wire electrodes (CWEs), one of the branches in ISEs, have drawn

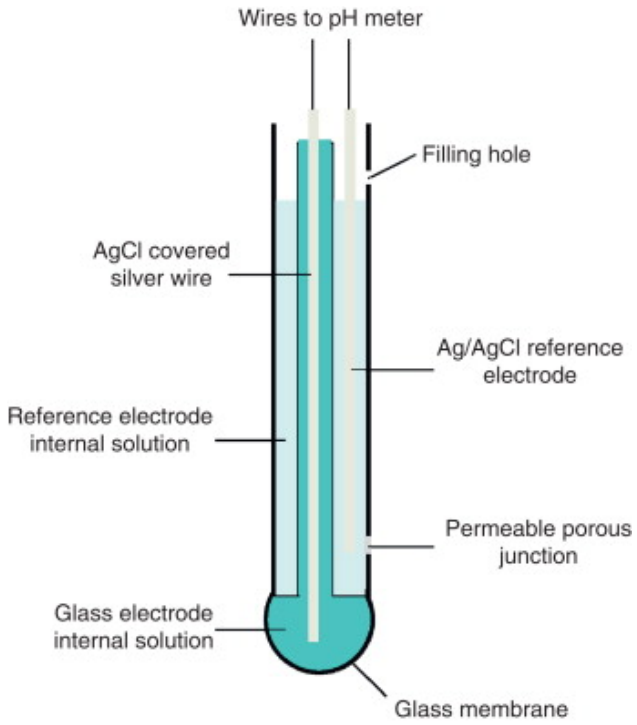

Figure 1.5 Typical glass electrode for pH measurement. Reprinted with permission from [30] © 2011 Elsevier B.V.

great attention from researchers. In the typical CWE design, a conductor is directly coated with an appropriate ion-selective polymer membrane to form an electrode system that is sensitive to electrolyte concentrations rather than using inner buffer solution and reference electrode internal solution as conventional ISE. Its response and detectability are similar to that of classical ISE. The great advantage is that the CWE design eliminates the need for an internal reference electrode, resulting in benefits during miniaturization [31]. It is widely used for the in vitro and in vivo biomedical and clinical monitoring of different kinds of analytes thanks to its simple structure and small size [32].

The ion-sensitive membranes used for ISEs are usually composed of three or four components: (1) polymeric matrix, (2) plasticizer, (3) lipophilic salt, and (4) ionophore, all matched in adequate proportions [33]. The composition of the ion-sensitive membrane dominates the sensitivity of the ISE. According to the membrane structure type, ISEs can be divided into five main classifications: (1) homogeneous crystalline membrane electrodes

(e.g., $AgCl/Ag_2S\ for\ Cl^-$); (2) heterogeneous crystalline membrane electrodes (e.g., silicone rubbers comprising crystalline powders such as LaF_3); (3) rigid noncrystalline membrane electrodes embodying silicate and chalcogenide glasses; (4) nonrigid noncrystalline electrodes employing plasticized polymer membranes incorporating neutral ionophores as receptor molecules; (5) sensitized electrodes such as carbon dioxide or ammonia ISEs separating a filling solution housing an immersed pH indicator electrode from the sample solution by a gas diffusion membrane [34]. Despite of the different crystalline structures, most ion-sensitive membranes are ionophore-based, containing ionophore and lipophilic salt (ion exchangers). Noted that it is the ion exchange process or ion transport process rather than the redox process that causes the analytical potential at the interface of the electrode coated with membrane. As the ion exchangers could be ionized into anions and cations, the membrane uses the ionized anions provided by ion exchangers to capture interest ions in the sample solution. The ionized cations move freely in the sample solution. Ionophores are lipophilic complexing agents that work as neutral carriers that cannot diffuse out of the membrane but can selectively bind ions with the formation of ion-to-ionophore complexes [33]. For instance, valinomycin is highly selective for potassium over sodium ions, it is the most frequently used natural ionophore. In nature, valinomycin is employed as a potassium ion-specific transporter through the cellular membrane, by binding and carrying the ions, resulting in reducing an electrochemical potential gradient across the membrane [35]. Therefore, as soon as the sample solution contacts the membrane, only the interest ions are permeable and will be caught by the ionophore. Then ions together with the anions group within the membrane will form complexes.

Apart from the ion exchange process contributed by the ion exchangers and ionophore, the diffusion of the interest ion also affects the potential at the membrane and reference electrode. As the interest ion diffuses from the high concentration to low concentration, excess cations tend to accumulate above the solution/membrane boundary while excess anions

gather underneath the solution/membrane boundary. Thus, a diffusion potential is developed across the membrane and solution. The electric force produced by anions in the membrane will oppose the diffusion force and eventually reaches a dynamic equilibrium between them. So, the potential difference will remain constant in the long term.

The ISE provides an electrochemical potential at the membrane that can be expressed by Nernst Equation as

$$\phi = \phi^0 + \frac{RT}{z_1 F} ln(a_1) \tag{1.1}$$

where ϕ is the ISE potential, ϕ^0 is the constant reference potential, R is the gas constant, T is the absolute temperature in Kelvin, F is the Faraday constant, z_1 is the valence of interest ion, and a_1 is the activity. The reference electrode is intended to build up a potential that does not depend on the composition of the ion to be measured. The difference of these potentials, electromotive force (EMF) between the indicator electrode and reference electrode, can be described by the Nikolsky equation as

$$E = E^0 + Slog\,(a_1) \tag{1.2}$$

where E is the desired EMF, E^0 is a fixed EMF value from the reference electrode, and S equals to $dE/dlog(a)$ which defines how much the measurement signal is changed when the ion concentration changes. Ionophores, ion exchangers, complexes stoichiometry, and the solvation of ions in plasticizers are major factors to the coefficients in Nikolsky equation [28].

1.4 Printed Electronics

Printed Electronics (PE), as the name implies, is one type of electronics manufactured by printing technology. This technology merges the fabrication process of electronic devices

with simplified printing steps. It aims to produce electronic devices and systems using simple printing methods instead of complex and expensive integrated circuit (IC) manufacturing technology. Especially PE is attractive for cost-effective manufacturing thanks to its features like simplified processing steps, reduced material wastage, low fabrication costs, and simple patterning techniques [36]. So far, PE on polymer substrates has opened new avenues for low-cost fabrication of electronics on areas larger than the standard wafers available commercially. On the other hand, researchers found that PE is compatible with a wide variety of flexible substrates for its lightweight and flexibility. This enables them to develop sensors for substrates with non-planner surfaces, which are difficult to realize with conventional wafer-based fabrication techniques. In recent decades, the development of electronic devices such as large-area printed pressure sensors [37], radio frequency identification tags (RFID) [38], and light emitting diodes (LED) [39] based on PE has illustrated its advancement in this field. Therefore, PE is more advantageous than the electronics fabricated with conventional IC techniques for its cost-effectiveness, lightweight, and flexibility.

A wide range of printing methods has already been applied to the manufacture of PE, including inkjet printing, screen printing, gravure printing, etc. They can be divided into two main categories depending on whether a template is employed or not; inkjet printing does not require any template while a template is necessary for screen printing and gravure printing. Different applications of PE have various demands on printing parameters such as ink preparation, printing resolution and accuracy, throughout and cost, wetting control and interface formation. This in turn limits the choice of printing method. In the subsections that follow, we will present a brief overview in the understanding of inkjet printing, screen printing, and gravure printing, including the working mechanism, pros, and cons for each printing method.

1.4.1 Inkjet Printing

Inkjet printing is a fast material-conserving deposition technique used for applications with a high accuracy requirement. An inkjet printer will first translate the circuit design layout file into a supported monochrome bitmap file. The printer control program then converts the monochrome image into a string of electrical pulses which drives the printer head and propel ink droplets. Afterward, the inkjet printer controls individual ink droplets precisely to come out of an ink nozzle, forming a pattern by the bitmap. There are two main modes of operations for droplet generators in inkjet printers; they can be classified as continuous inkjet (CIJ) and drop on demand inkjet (DOD). Each mode has its particular requirements for the physical properties of the ink and a characteristic drop size range.

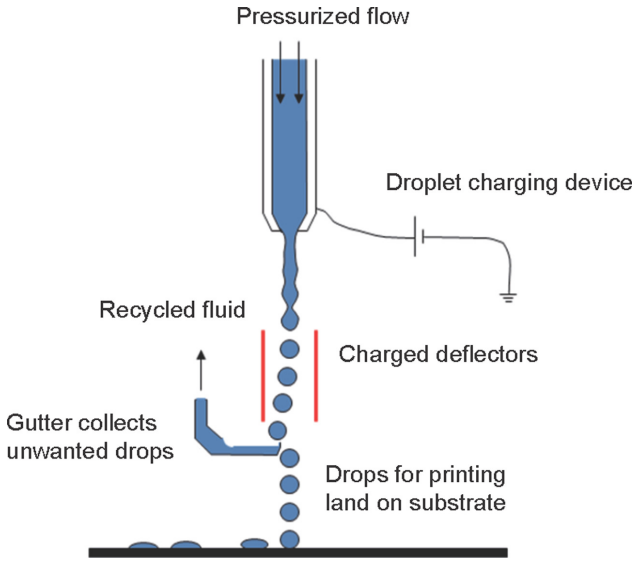

Figure 1.6 Schematic illustration of the operating principles of a continuous inkjet printer (CIJ). Reprinted with permission from [40] © 2015 Elsevier

Figure 1.6 shows the schematic illustration of the operating principle of the CIJ printer. A CIJ printer produces a continuous stream of drops under pressurized flow; unwanted droplets will be deflected into a gutter through charged deflectors and then be recycled to prevent waste. The diameter of the droplet is slightly larger than the diameter of the nozzle. CIJ produces a greater volume of ink per unit time among two modes of operation and

has a faster printing speed. The main drawback of this mode is that the continuous fluid jetting leads to significant ink wastage and, if recirculation is used, the potential for ink contamination [40].

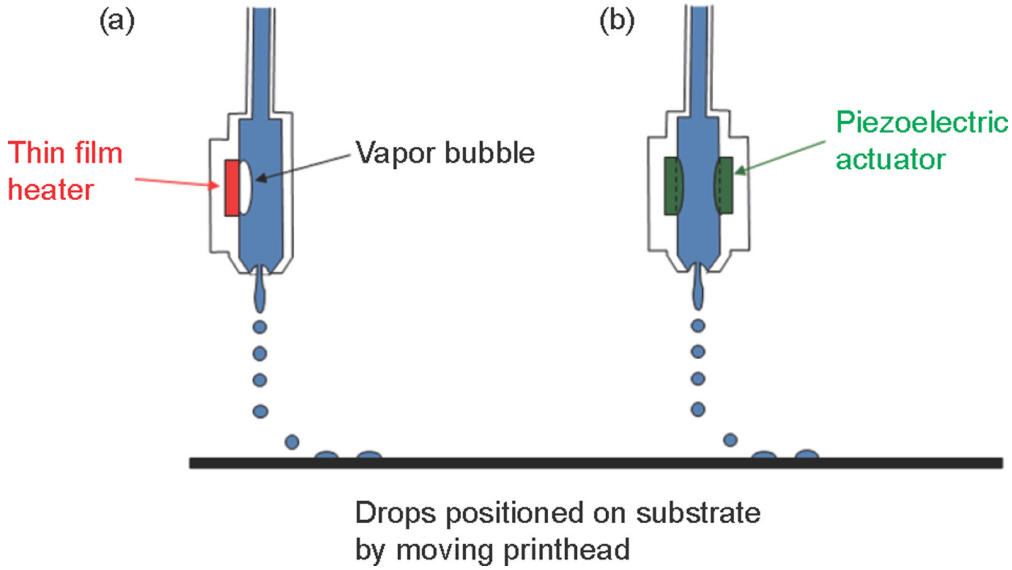

Figure 1.7 Schematic illustration of the operating principles of a drop-on-demand inkjet printer (DOD) with (a) thermal and (b) piezoelectric actuation. Reprinted with permission from [40] © 2015 Elsevier

Figure 1.7(a) and Figure 1.7(b) illustrate the working principle of a DOD printer with thermal and piezoelectric actuation respectively. DOD printer only drops ink droplets on the substrate when required. This printing process essentially involves the ejection of a fixed quantity of ink in a reservoir from the nozzle through a sudden pressure pulse. This pressure pulse must overcome the surface tension forces that hold the liquid drops in place; the resulting ejected column of liquid is pinched off to form a drop by a combination of surface tension forces and return flow of the liquid in the reservoir [40]. The pressure pulse can be formed either mechanically by a piezoelectric actuator or by the formation and collapse of a vapor pocket in the ink through local heating. The ejected drop will fall under action of gravity and air resistance until it impinges on the substrate, spreads under momentum acquired in the motion, and surface tension aided flow along the surface [41]. Compared

with the CIJ printer, the DOD printer has a much simpler inkjet structure and a lower cost. The main concern of the DOD printer is the lower durability of the printer head and a limited choice of ink. For instance, a low boiling-point ink is mandatory for the thermal DOD printer to ensure the formation of the vapor pocket.

1.4.2 Screen Printing

Screen printing is one of the commonly used replicate printing methods in the industry. It requires a template (screen mask) instead of a bitmap file controlled by a program to determine the size and pattern of the proposed circuit design. The screen printer allows for thick film patterns to be manufactured. The ink for screen printing is usually of high viscosity to ensure it will not leak onto the substrate without a squeeze press. It is normally composed of graphite, carbon, gold, silver, platinum, binders, polymers, plasticizers, solvents, additives such as metals, metal oxides, enzymes, and ion exchangers [42]. When the fluid comes in contact with the substrate, it returns to its original viscosity, forming the desired pattern.

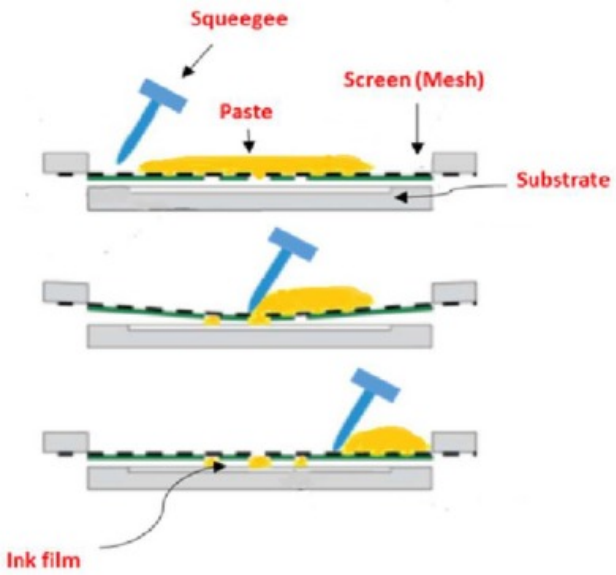

Figure 1.8 Schematic diagram of the screen printing basic process. Reprinted with permission from [42] © 2016 Elsevier B.V.

A Schematic diagram of the screen printing basic process is illustrated in Figure 1.8. The

screen mask is composed of a frame, a fabric mesh, and a light-sensitive stencil on the mesh. The pattern of the screen mask is realized via the patterned stencil by optical lithography. After making the screen mask, the printing process can initiate by covering the ink paste above the screen mask and placing the substrate underneath it. Then, a squeegee will move across the screen and forces the paste to penetrate through the patterned area to deposit on the substrate. Therefore, the printed paste on the substrate can replicate exactly the pattern of the screen. The overall cost of screen printing is low for its replicability, and the printing operation can be easily controlled via squeegee movement as the ink has high viscosity. However, it is constrained to the ink with high viscosity, and it usually supports layout with low resolution due to the rough pattern surface.

1.4.3 Gravure Printing

Gravure printing is a widely used industrial printing technique that is capable of producing prints of outstanding quality consistently. A gravure printer consists of a gravure cylinder, an ink fountain, a doctor blade, and an impression cylinder. The working principle of gravure printing is shown in Figure 1.9. Before printing, the surface of the gravure cylinder is immersed in the ink fountain. A doctor blade will remove the excess ink from the area of nonimage elements. Then, the ink remained in the engraved area will be transferred onto the surface of the substrate by the impression cylinder in contact with the gravure as a consequence of high pressure and the adhesive force between the ink and the substrate [43].

The inks for gravure printing are usually of low viscosity without additives; they are mainly water- and solvent-based inks. Inks with solvents are recommended, as they dry faster and the printing process is shorter [43]. The speed of the gravure printer is very fast, which can lead to the occurrence of missing dots. As explained in Rozalia's research [43], missing dots can occur when the contact between the printing ink and the substrate is not appropriate, or due to the high roughness or low compressibility of the substrate, etc.

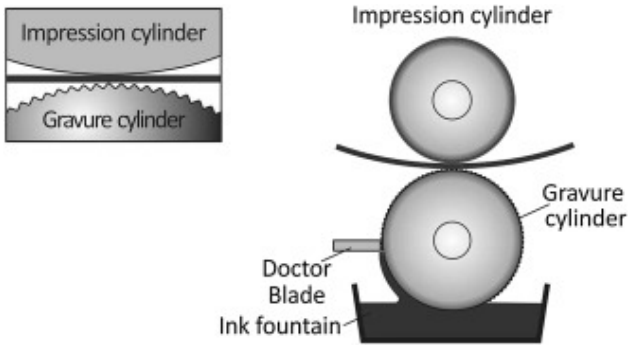

Figure 1.9 Wokring principle of gravure printing. Reprinted with permission from [43] © 2016 Elsevier Inc.

Besides, the price of the gravure printer is expensive and the layout of the gravure cylinder is hard to modify. So, it is only suitable for large quantities of products and is too costly for the prototype designs.

An overview of the advantages and disadvantages of three different printing techniques is presented above. It is necessary to choose the appropriate printer for a specific PE design. After the deposition of ink on the substrate, the printed layout needs to be baked in a high-temperature environment to get rid of the surfactant and solvent in ink via evaporation. This is the inevitable sintering process. After the sintering process, the fabrication of a PE design is almost finished, and manufactor can move on to the testing process to verify the design target.

1.5 Research Motivation

This thesis presents a flexible printed RFID sensor for remote K^+ detection. The entire RFID sensor consists of a passive inductive-capacitive (LC) resonator and an ion-selective electrode (ISE). The main motivation for my research is the importance of developing a cost-effective and flexible wireless passive K^+ sensor technology for low cost K^+ monitoring applications like food package monitoring. As delineated above, it is important to maintain a normal level of K^+ in the human body. Thus, a simple and cost-effective K^+ detection

technique is preferred for monitoring levels of K^+ in food and drinking water packages/sample. Another important drive is the drawbacks of some early developed ISE-based chemical potassium sensors such as high cost, poor miniaturization, and limited durability. These problems will be discussed in detail later in this thesis. The printed electronic (PE) technology is preferred for the fabrication of the sensor. Compared to traditional IC microfabrication techniques, it has the advantage of less material wastage, low cost, better compatibility, and high throughput. So far, PE has already demonstrated its effective performance in numerous applications, such as the thin-film transistor (TFT), biomedical sensor, and antenna design [44].

Therefore, the objective is to develop a printed simple and cost-effective LC and ISE based wireless passive K^+ sensor, illustrate an appropriate interrogation method where the sensor may be attached to a flexural medium, measure the wireless response of the sensor for samples with different K^+ concentration, determine the sensor's operating range, accuracy, response, long-term stability, and temperature stability. The eventual wireless passive RFID sensor prototype should have the advantages of low fabrication and operation cost. It should be especially suitable for applications where direct electrical connection is inconvenient or impossible, since no power supply is required.

1.6 Thesis Structure

This thesis is composed of six chapters. Chapter 1 is about the background introduction and literature review of this thesis. It includes the importance of potassium ion sensing, the overview of RFID technology, the basics of ion sensitive electrodes, the overview of printed electronics, and research motivation. Chapter 2 will present the transmission line theory and scatter parameters. It will also introduce three different printed inductor designs: straight line, single-loop circular, and spiral inductor as well as the printed interdigital capacitor design. Chapter 3 will discuss the ion selective membrane solution and K^+ ion selective

electrode. Chapter 4 will describe the design of two printed LC resonators on FR4 and Kapton substrate respectively and the interrogator coil design. Chapter 5 will demonstrate the design, measurement, and modification of a flexible printed LC resonator based RFID sensor for remote K+ detection. It will illustrate the sensor's wireless performance, operating range, accuracy, response, long-term stability, and temperature stability. Chapter 6 will illustrate the modified RFID sensor design and its performance improvement. Eventually, Chapter 7 will conclude this thesis and discuss future work.

Chapter 2

Printed Inductor and Capacitor Design

2.1 Review on Transmission Model Analysis

2.1.1 Lumped Element Model Analysis

The wireless performance of the proposed RFID sensor is designed to be measured using the interrogator coil via a Vector Network Analyzer (VNA). The corresponding scattering parameters for each trial will be obtained as the key parameter for further analysis. To facilitate the discussion of scattering parameters in later chapters, it is necessary to discuss the fundamental background needed to understand the concept of scattering parameters. Therefore, it is beneficial to review some transmission model theories that are directly related to the definition of scattering parameters in the network. Most of the following formulas can be found and derived from [45].

A lossy transmission line can be modelled as a distributed parameter circuit consisting of a couple of small segments of length Δz shown in Figure 2.1. The above line represents the conductor line is for signal propagation, and the bottom one is the signal ground so

that the structure is closed-loop. The lumped element model of each segment describing the transmission line are:

r: series resistance of the transmission line per unit length (Ω/m)

l: series inductance of the transmission line per unit length (H/m)

g: shunt conductance between two conductors per unit length (S/m)

c: shunt conductance between two conductors per unit length (F/m)

Noted that the series resistance r and inductance l is due to the finite conductivity and self-inductance of the conductors respectively; the conductance g is caused by the dielectric losses between two conductors; the shunt capacitance c is caused by the proximity of two conductors, analogy to a parallel plate capacitor.

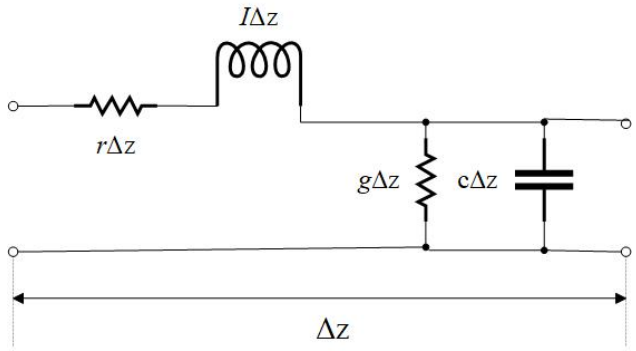

Figure 2.1 Circuit Model of a lossy transmission line

It is helpful to consider an ideal lossless transmission line first before moving on to the analysis lossy transmission line in reality. Figure 2.2 shows a single segment of a lossless transmission line.

The analysis can start by applying Kirchhoff's voltage law around the outside loop. The derived equation is

$$V\left(z+\Delta z,t\right)-V\left(z,t\right)=-l\Delta z\frac{\partial I\left(z,t\right)}{\partial t}. \tag{2.1}$$

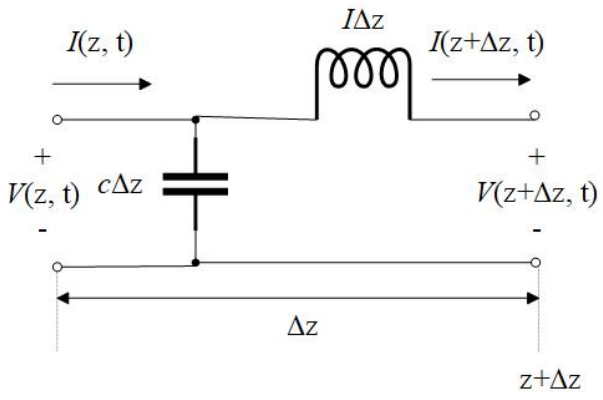

Figure 2.2 Circuit Model of a lossless transmission line

Dividing both sides by Δz and then taking the limit provides

$$\lim_{\Delta z \to 0} \frac{V(z+\Delta z, t) - V(z,t)}{\Delta z} = -l\frac{\partial I(z,t)}{\partial t} \tag{2.2}$$

$$\frac{\partial V(z,t)}{\partial z} = -l\frac{\partial I(z,t)}{\partial t}. \tag{2.3}$$

Similarly, writing Kirchhoff's current law at the upper node of the capacitor results in

$$I(z+\Delta z, t) \; - I(z,t) = -c\Delta z \; \frac{\partial V(z+\Delta z, t)}{\partial t}. \tag{2.4}$$

Dividing both sides by Δz and then taking the limit provides

$$\frac{\partial I(z,t)}{\partial z} = -c\frac{\partial V(z,t)}{\partial t}. \tag{2.5}$$

Differentiating Eqn. 2.3 with respect to z and differentiate Eqn. 2.5 with respect to t, we can get

$$\frac{\partial^2 V(z,t)}{\partial z^2} = -l\frac{\partial^2 I(z,t)}{\partial t \partial z} \tag{2.6}$$

$$\frac{\partial^2 I(z,t)}{\partial z \partial t} = -c\frac{\partial^2 V(z,t)}{\partial t^2}. \tag{2.7}$$

Substituting Eqn. 2.7 into Eqn. 2.6, we can get the first transmission line equation as

$$\frac{\partial^2 V(z,t)}{\partial z^2} = lc\frac{\partial^2 V(z,t)}{\partial t^2}. \tag{2.8}$$

Similarly, the second transmission line equation can be derived as

$$\frac{\partial^2 I(z,t)}{\partial z^2} = lc\frac{\partial^2 I(z,t)}{\partial t^2}. \tag{2.9}$$

The general solutions to these transmission line equations are

$$V(z,t) = V^+\left(t - \frac{z}{v}\right) + V^-\left(t + \frac{z}{v}\right) \tag{2.10}$$

$$I(z,t) = I^+\left(t - \frac{z}{v}\right) + I^-\left(t + \frac{z}{v}\right) \tag{2.11}$$

where

$$I^+\left(t - \frac{z}{v}\right) = \frac{1}{Z_c}V^+\left(t - \frac{z}{v}\right) \tag{2.12}$$

$$I^-\left(t + \frac{z}{v}\right) = -\frac{1}{Z_c}V^-\left(t + \frac{z}{v}\right) \tag{2.13}$$

and Z_c is the characteristic impedance of the line defined as

$$Z_c = \sqrt{\frac{l}{c}}. \tag{2.14}$$

The expression $V^+(t - \frac{z}{v})$ represents a forward-traveling voltage wave traveling in the $+z$ direction, while the function $V^-(t+\frac{z}{v})$ represents a backward-traveling voltage wave traveling in the $-z$ direction.

Similar logic and deduction process can be used on the lossy transmission line. Starting from the KVL to the outer loop of the circuit in Fig. 1 and we can get the transmission line

equations written in the form

$$\frac{d^2\hat{V}(z)}{dz^2} - \hat{\gamma}^2\hat{V}(z) = 0 \tag{2.15}$$

$$\frac{d^2\hat{I}(z)}{dz^2} - \hat{\gamma}^2\hat{I}(z) = 0 \tag{2.16}$$

where $\hat{\gamma}$ is the propagation constant defined by

$$\hat{\gamma} = \sqrt{(r+jwl)(g+jwc)} = \alpha + j\beta \approx \frac{\sqrt{lc}}{2}\frac{rc+lg}{lc} + jw\sqrt{lc} \tag{2.17}$$

and α is the attenuation constant and β is the phase constant. The general solution consists of the forward and backward traveling waves can be written as

$$\hat{V}(z) = \hat{V}_f(z) + \hat{V}_b(z) \tag{2.18}$$

$$\hat{I}(z) = \hat{I}_f(z) + \hat{I}_b(z) \tag{2.19}$$

where

$$\hat{V}_f(z) = \hat{V}^+ e^{-\alpha z} e^{-j\beta z} \tag{2.20}$$

$$\hat{V}_b(z) = \hat{V}^- e^{\alpha z} e^{j\beta z} \tag{2.21}$$

$$\hat{I}_f(z) = \frac{\hat{V}^+}{\hat{Z}_c} e^{-\alpha z} e^{-j\beta z} \tag{2.22}$$

$$\hat{I}_b(z) = -\frac{\hat{V}^-}{\hat{Z}_c} e^{\alpha z} e^{j\beta z} \tag{2.23}$$

and $\hat{Z}_c$ is the complex characteristic impedance given by

$$\hat{Z}_c = \sqrt{\frac{\hat{z}}{\hat{y}}} = \sqrt{\frac{r+jwl}{g+jwc}}. \tag{2.24}$$

To sum up, the expressions for characteristic impedance Z_c, propagation constant γ, attenuation constant α, and phase constant β for both lossless and lossy transmission lines are listed separately in Table 2.1.

Table 2.1 Summary of lossy and lossless transmission lines

	Z_c	γ	α	β
Lossless	$\sqrt{\frac{l}{c}}$	$jw\sqrt{lc}$	0	$w\sqrt{lc}$
Lossy	$\sqrt{\frac{r+jwl}{g+jwc}}$	$\sqrt{(r+jwl)(g+jwc)}$	$\frac{\sqrt{lc}}{2}\frac{rc+lg}{lc}$	$w\sqrt{lc}$

2.1.2 Scattering Parameters

For a low-frequency network system, we can obtain the relevant information about the network by taking either short or open circuit measurements at its port to get the equivalent circuit model. However, in a high-frequency domain, the spatial, time-variant voltage and currents are noticeably affected by the parasitic inductance and capacitance, making the truly open and truly short state at each port formidable. Therefore, it is more convenient and effective to characterize a high-frequency network from the concept of the wave. Since the wave at any point can be split into forwarding and backward waves, making it straightforward for the measurement in the steady-state condition. Based on wave measurement at each port, researchers come up with the ideology of scattering parameters (s-parameter).

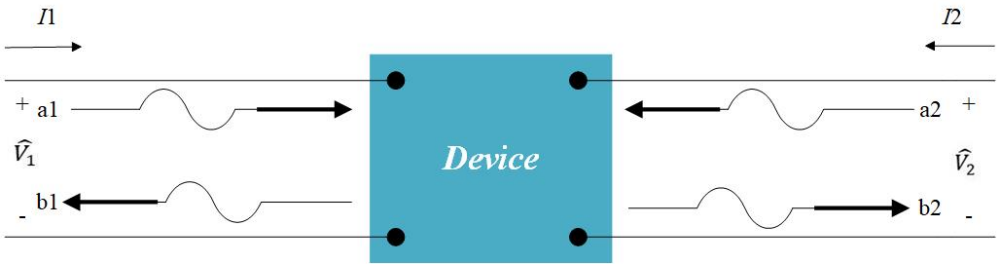

Figure 2.3 Incident and reflected waves at the two-port system

A two-port network connected to a transmission line with incident waves (a_1, a_2) and

reflection waves (b_1, b_2) is shown in Figure 2.3. The incident and reflected waves can be used to define s-parameters for this network. The linear equations describing this two-port network in terms of the s parameters are defined as

$$b_1 = s_{11}a_1 + s_{12}a_2 \tag{2.25}$$

$$b_2 = s_{21}a_1 + s_{22}a_2. \tag{2.26}$$

The incident and reflected waves are related to the voltage and current waves at each port as

$$a_1 = \frac{\hat{V}_1 + \hat{Z}_c\hat{I}_1}{2\sqrt{Z_c}} = \frac{V_{i1}}{\sqrt{Z_c}} \tag{2.27}$$

$$b_1 = \frac{\hat{V}_1 - \hat{Z}_c\hat{I}_1}{2\sqrt{Z_c}} = \frac{V_{r1}}{\sqrt{Z_c}} \tag{2.28}$$

$$a_2 = \frac{\hat{V}_2 + \hat{Z}_c\hat{I}_2}{2\sqrt{Z_c}} = \frac{V_{i2}}{\sqrt{Z_c}} \tag{2.29}$$

$$b_2 = \frac{\hat{V}_2 - \hat{Z}_c\hat{I}_2}{2\sqrt{Z_c}} = \frac{V_{r2}}{\sqrt{Z_c}} \tag{2.30}$$

where V_{i1}, V_{i2} are the incident voltage waves, and V_{r1}, V_{r2} are the reflected voltage waves at ports 1 and 2 respectively.

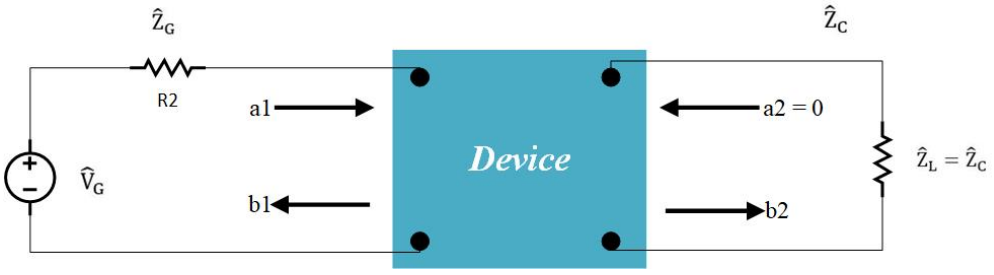

Figure 2.4 Two-port device driven at port 1 and terminated by a load at port 2

Figure 2.4 depicts a typical two-port device driven at port 1 and terminated by a load at port 2. After the source voltages applied at port 1, the incident wave $\hat{a}_1$ will first arrive at

port 1 where it creates a reflected wave $\hat{b}_1$ and a transmitted wave $\hat{b}_2$. The reflected wave $\hat{b}_1$ will go back to the source. If the source is matched to the transmission line ($\hat{Z}_G = \widehat{Z}_c$), there is no reflection at the source and thus no other wave will travel to port 1. The transmitted wave $\hat{b}_2$ will reach the load connected to port 2. If the load is not matched to the transmission line ($\hat{Z}_L \neq \widehat{Z}_c$), a reflection will happen and a reflected wave $\hat{a}_2$ will travel towards port 2. However, if the load is matched to the transmission line, no reflection occurs at the load and thus no wave will be incident on port 2.

The individual s-parameters can be derived with proper termination at ports. S11 is the input port reflection coefficient when the incident wave at port 2 is zero, which means that port 2 should be terminated in a match load ($\hat{Z}_L = \widehat{Z}_c$) to avoid reflection. It can be obtained as $S11 = \frac{b_1}{a_1}|_{a_2=0}$. $S21 = \frac{b_2}{a_1}|_{a_2=0}$, which describes the transmission coefficient from port 1 to port 2 with port 2 terminated in a matched load. Similarly, $S22 = \frac{b_2}{a_2}|_{a_1=0}$ and $S12 = \frac{b_1}{a_2}|_{a_1=0}$ are the output port reflection coefficient and transmission coefficient from port 2 to port 1 respectively. Noted that S11 is also known as the return loss, which represents how much power is reflected from the antenna. If S11=0 dB, then all the power is reflected from the antenna and nothing is radiated. S21 represents the gain of the load if it is active, or the insertion loss of the load if it is passive.

2.2 Printed inductor Design

The printed passive components have been widely applied in passive RFID designs for their flexibility and low cost. There are several design models for the implementation of inductors and capacitors. It is beneficial to briefly review the lumped model of passive component designs before moving onto the integrated RFID design. Starting from the printed inductor designs, the analysis of the straight-line inductor, single-loop inductor, and spiral square inductor is illustrated separately as following.

2.2.1 Straight-Line Inductor

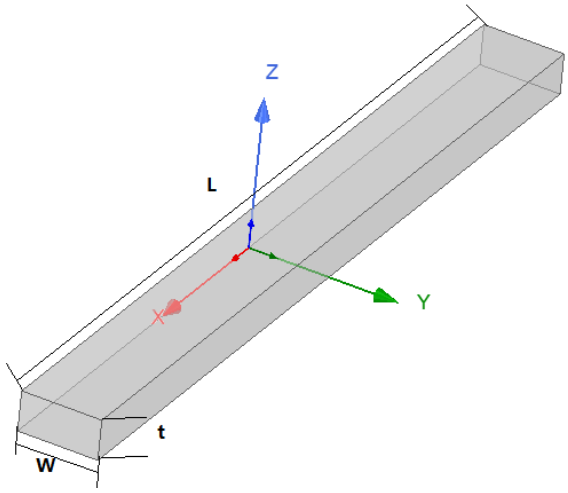

Figure 2.5 Straight line inductor

Figure 2.5 shows the layout of a straight-line inductor. The self-inductance of the line inductor is defined as the double volume integral of the scalar product of the current density vector $\vec{J_1}(\vec{r_1})$ and $\vec{J_2}(\vec{r_2})$ at the points $\vec{r_1}$ and $\vec{r_2}$ divided by the distance r_{12} between these points [46]. The inductance expression of the whole conductor in a vacuum environment is given by

$$L = \frac{\mu_0 L}{4\pi I^2} \iint \vec{J_1} \bullet \vec{J_2} \frac{d\tau_1 d\tau_2}{r_{12}} \tag{2.31}$$

where $d\tau_1$ and $d\tau_2$ are the volume elements around the investigation points $\vec{r_1}$ and $\vec{r_2}$ respectively, μ_0 is the magnetic permeability of the vacuum, and I is the total current flowing in the conductor. For simplicity, assuming a simple length of straight conductor with zero metallization thickness t, the self-inductance could be found by

$$L = \frac{\mu_0 L}{2\pi} \left\{ arcsinh(\frac{L}{W}) + (\frac{L}{W}) arcsinh(\frac{W}{L}) + \frac{W}{3L} - \frac{1}{3}(\frac{L}{W})^2 \left[(1 + \frac{W^2}{L^2})^{\frac{3}{2}} - 1 \right] \right\} \tag{2.32}$$

where W is the conductor line width and L represents line length [47]. Noted that if the line width W is much larger than the metallization thickness t, the influence of thickness could simply be estimated by replacing the line width W by $(W+t)$ in the above expression. However, when the line width and the thickness are of the same order, the above expression is invalid. Ollendorff [48] has found the analytical formulae of the straight-line inductor with rectangular cross-section using the medium geometrical distance method by

$$L = \frac{\mu_0 L}{2\pi}[ln(\frac{2L}{\rho}) - 1] \tag{2.33}$$

$$ln(\frac{\rho}{2c}) = -\frac{25}{12} - \frac{1}{6}\left\{\left(\frac{W}{t}\right)^2 ln\sqrt{1+\left(\frac{t}{W}\right)^2} + \left(\frac{t}{W}\right)^2 ln\sqrt{1+\left(\frac{W}{t}\right)^2}\right\} + \frac{2}{3}\left\{\frac{W}{t}arctan\left(\frac{t}{W}\right) + \frac{t}{W}arctan\left(\frac{W}{t}\right)\right\} \tag{2.34}$$

$$c = \frac{\sqrt{W^2+t^2}}{2} \tag{2.35}$$

The above formulae work properly for homogenous current density over the cross-section of the straight-line inductor. In practice, the skin effect would lead to frequency-dependent current density over the cross-section. However, the skin effect would only affect the inner conductance and the inner conductance is negligibly small compared with the total inductance [47]. Therefore, we could ignore the skin effect in this case. The straight-line inductor is easy to fabricate due to a simple structure but suffers from low overall inductance. Since the overall inductance is mainly comprised of self-inductance and limited mutual inductance effects are included.

2.2.2 Single Turn Circular Loop Inductor

Moving on to complicated inductor designs with more loops. First, considering a single-turn inductor with a circular ring section. The geometry of a single turn circular loop inductor of the outer radius R_{out} , inner radius R_{in} , and circular arc angle φ_0 is illustrated

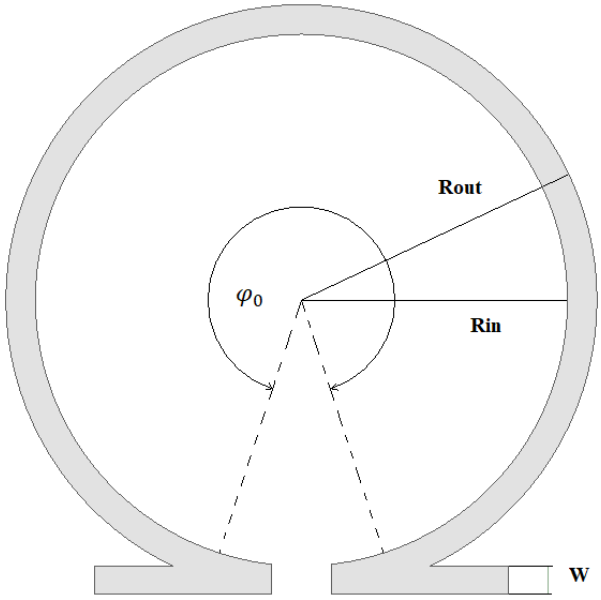

Figure 2.6 Single turn Circular Loop Inductor

in Figure 2.6. The self-inductance of the circular loop inductor is described by the volume integral of the current density vector $\vec{J_1}(\vec{r_1})$ and $\vec{J_2}(\vec{r_2})$ at the points $\vec{r_1}$ and $\vec{r_2}$ over their cross-sections along the arc angle φ_0. Considering the case of zero metallization thickness, Pattenpaul et al. [47] showed that the inductance expression could be reduced to a fourfold integral

$$L = \frac{\mu_0}{4\pi w^2} \int_{R_{in}}^{R_{out}} \int_{R_{in}}^{R_{out}} \int_0^{\varphi_0} \int_0^{\varphi_0} H dr_1 dr_2 d\varphi_1 d\varphi_2 \tag{2.36}$$

with

$$H = \frac{r_1 r_2 cos(\varphi_2 - \varphi_1)}{\sqrt{{r_1}^2 + {r_2}^2 - 2r_1 r_2 cos(\varphi_1 - \varphi_2)}}. \tag{2.37}$$

The fourfold integral could not be solved numerically easily. Efforts were made by Pattenpaul et al. to simplify the calculation. As a result, Pattenpaul et al [47] proposed an onefold

integral for straight numerical calculation as following

$$L = \frac{\mu_0}{4\pi w^2}\int_0^{\varphi_{0/\sqrt{2}}} (\varphi_0\sqrt{2} - 2\varphi)cos(\sqrt{2}\varphi)F(\varphi)d\varphi. \tag{2.38}$$

$F(\varphi)$ is defined by

$$F(\varphi) = G(r_1, r_2)|_{r_1=r_i}^{r_0}|_{r_2=r_i}^{r_0} = G(r_0, r_0) - G(r_i, r_0) - G(r_0, r_i) + G(r_i, r_i) \tag{2.39}$$

where

$$G(r_1, r_2) = \frac{1}{3}R^3 + \frac{2}{3}r_1r_2Rcos(\sqrt{2}\varphi) + \frac{2}{3}{r_1}^3cos(\sqrt{2}\varphi) \bullet arsinh\frac{r_2 - r_1cos(\sqrt{2}\varphi)}{r_1\left|sin(\sqrt{2}\varphi)\right|} \tag{2.40}$$

$$R = \sqrt{{r_1}^2 + {r_2}^2 - 2r_1r_2cos(\sqrt{2}\varphi)} \tag{2.41}$$

Similar to the case of the single-line inductor, when metallization thickness t is much smaller than the line width W, the influence of thickness could simply be estimated by replacing the line width W by $(W + t)$ in the above expression.

The above expression describes the ideal situation of a single-turn circular loop inductor with limited conductor thickness. In practice, the inductance of printed single turn circular loop inductor may be affected by other elements such as the capacitive effect of ground metallization, shape of conductor cross-section, etc. These factors would introduce extra frequency-dependent parameters for the loop inductor. Concerning the layout printed by the common inkjet printer, the conductor cross-section would be tubular. Terman [49] provided the inductance approximation of a single-turn circular loop inductor with the tubular cross-section at both low and high frequencies. Based on Terman's work [49], the low-frequency inductance (μH) of a tube of the inner diameter d_{in} and outer diameter d_{out}, bent into a

circle of mean diameter D inches, is

$$L_0 = 0.01595D\ [2.303log_{10}\frac{8D}{d_{out}} - 1.75 - \frac{{d_{in}}^2}{2({d_{out}}^2 - {d_{in}}^2)} + 2.303\frac{{d_{in}}^4}{({d_{out}}^2 - {d_{in}}^2)^2}log_{10}\frac{d_{out}}{d_{in}}] \tag{2.42}$$

and the high-frequency assumption is given as

$$L_\infty = 0.01595D\left(2.303log_{10}\frac{8D}{d_{out}} - 2\right). \tag{2.43}$$

Generally, compared to the single-line inductor, the single-turn circular loop inductor has a higher level of self conductance magnitude of a few microhenries due to the mutual inductance of different loop segments. But in return, the layout of the single-turn circular loop inductor requires a more complicated fabrication process and the inductance magnitude varies more at different frequencies. It is noted that the usage of the single-turn circular loop inductor deeply relies on the exact working frequency of the overall circuit.

2.2.3 Spiral Inductor

Planner square spiral inductors have been commonly used in printed circuits for their well-defined inductance and ease of layout. A specific square spiral conductor could be generated given a couple of parameters: the turn width w, number of turns n, turn spacing s, and inner diameter d_{in}. The thickness of the conductive segments usually has few effects on inductance and thus could be ignored.

The layout of a typical square spiral inductor is shown in Figure 2.7. As the inductor consists of many turns of conductive segments, the self-inductive and mutual-inductive effects in each segment would lead to phase shift leading to the impressed conductive current. Meanwhile, the presence of the substrate and closely spaced segments will cause the accumulation and flow of charge at the surface of the substrate and neighboring segments. Furthermore,

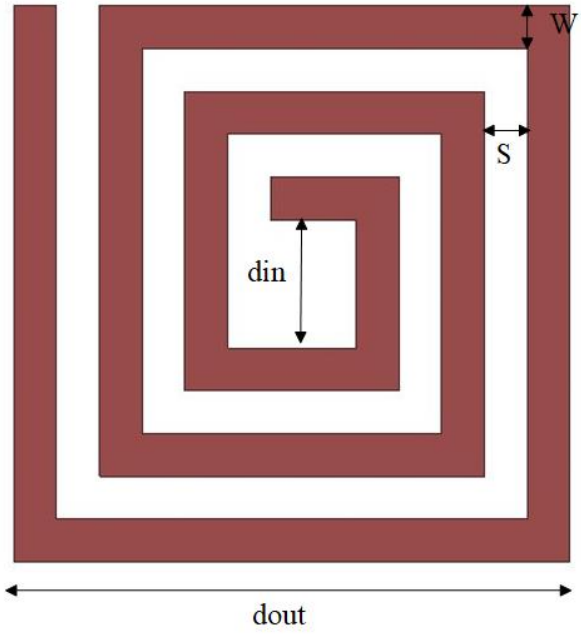

Figure 2.7 Planner Square Spiral inductor

the finite conductivity of the substrate is another source of loss. Since the induced substrate charge would flow through the lossy substrate.

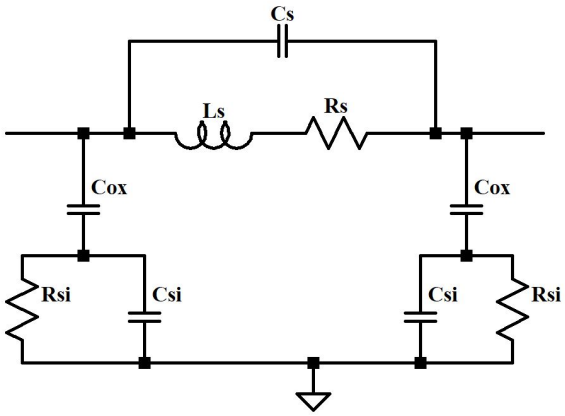

Figure 2.8 Lumped spiral inductor model

Figure 2.8 illustrates a lumped model of the square spiral inductor. In this plot, L_s models the overall inductance of the spiral combining all sources of inductive reactance.

It is frequency-dependent as the magnetic field and current distribution in each segment will change due to skin-effect and proximity effect of neighboring segments at different frequencies. R_s represents the loss due to the finite conductivity of the metal segments. The interwinding capacitance C_s is lossy since segments are linked through the substrate. At lower frequency, when the substrate acts as a good ground plane, the substrate will partially shield segments from each other. But at a higher frequency, due to the finite time constant of the substrate, as well as the non-zero impedance that grounds the substrate externally, the substrate will begin to float electrically. In this situation, the substrate will not shield metal segments as effectively, and the effective coupling capacitance will increase. C_{ox} and C_{si} models the capacitance from the metal segments to the substrate. R_{si} represents the substrate loss. They are all frequency-dependent due to the frequency dependence of substrate conduction.

Noted that the outer segments of the spiral are longer and have more volume to support fringing fields whereas inner turns are shorter and less capacitive [50]. The outermost turn has additional volume for fringing fields outside of the area of the spiral itself. This would tend to make the outer part of the spiral more capacitive.

The lumped inductor model is hard to describe in an accurate and simple expression. To solve this problem, significant work has gone into modeling the approximate inductance using simple expressions. For example, Wheeler [51] presented several formulas that allow us to obtain an approximation expression for planar spiral inductors

$$L_{mw} = K_1 \mu_0 \frac{n^2 d_{avg}}{1 + K_2 \rho} \tag{2.44}$$

$$\rho = \frac{(d_{out} - d_{in})}{(d_{out} + d_{in})} \tag{2.45}$$

$$d_{avg} = 0.5 \times (d_{out} + d_{in}), \tag{2.46}$$

where coefficients K_1=2.34, K_2=2.75, which are layout dependent. The average diameter

d_{avg} and fill ratio ρ could be computed using the inner diameter d_{in} and outer diameter d_{out} respectively. Noted that the high fill ratio would lead to a significant decrease in spiral inductor inductance. As the inner turns are closed to each other, they would contribute to more negative mutual inductance. Another expression based on current sheet approximation is presented in the following equation,

$$L_{square} = \frac{n^2 d_{avg} c_1 \mu_0}{2} \left[ln(\frac{c_2}{\rho}) + c_3\rho + c_4\rho^2 \right], \tag{2.47}$$

where the layout-dependent coefficients c_1=1.27, c_2= 2.07, c_3=0.18, and c_4=0.13 respectively. It has the advantages of simplicity and accuracy.

Overall, the printed spiral inductor has two distinct advantages; high link efficiency and a smaller size that increases the feasibility of placement in various biomedical applications [52]. It is also more flexible for design optimization since the total inductance can be modified easily by changing the number of loops and the aspect ratios. The target final RFID sensor has a request of small size and its self-inductance should be strong enough for inductive coupling. Therefore, a planner square spiral inductor is chosen for the LC resonator configuration for its efficiency and compact size.

2.3 Printed Capacitor Design

Interdigital capacitors are the most commonly used structures in the field of microelectronic, especially for the realization of RF/Microwave applications. Interdigital capacitor (IDC), as a type of passive component with multiple interdigital fingers, is widely used for the application of RFID sensors such as humidity sensors, gas sensors, etc [53, 54]. The printed interdigital planar capacitors are especially preferred for high-frequency applications thanks to their flexibility. For example, Molina-Lopez et al. [55] have proved the feasibility of inkjet-printed interdigital capacitors on flexible materials such as polyetherimide (PEI)

and polyimide (Kapton) substrates.

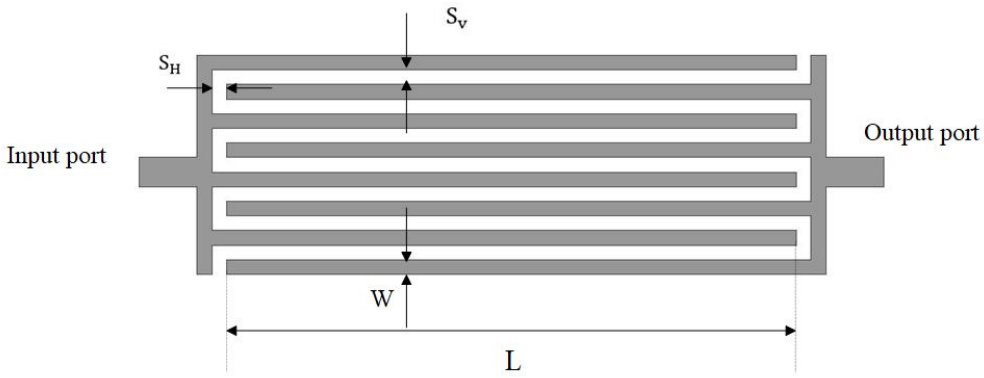

Figure 2.9 Layout of a typical interdigital capacitor.

The layout of a typical interdigital capacitor is shown in figure 2.9. The total capacitance of the interdigital capacitor is regulated by its physical parameters: finger width (w), finger spacing (s), finger length (l), and the number of fingers (N). These parameters can be varied individually for the desired capacitance of particular applications. Noted that the finger width and space width need to be equal for maximum capacitance density. And the area of IDC should be small relative to the wavelength so that it can be treated as a lumped element.

The properties of planar IDC have been studied by many authors [56, 57, 58]. An approximation equation for IDC's capacitance in the low-frequency domain is given by [56]

$$C = (\varepsilon_r + 1)l[(N-3)A_1 + A_2](pF) \tag{2.48}$$

where ε_r is the dielectric constant of the substrate material and l is the finger length. A_1 and A_2 are variables for interior and exterior fingers respectively and are provided as

$$A_1 = 4.409tanh[0.55(\frac{h}{W})^{-0.45}] \times 10^{-6}(pF/\mu m) \tag{2.49}$$

$$A_2 = 9.92tanh[0.52(\frac{h}{W})^{-0.45}] \times 10^{-6}(pF/\mu m) \tag{2.50}$$

where h represents the height of the substrate and W represents the width of the conductor segment.

In the high-frequency domain, the loss due to series resistance and the effect of parasitic capacitance and inductance should not be ignored. Figure 2.10 demonstrates the equivalent circuit model of the IDC at high frequency

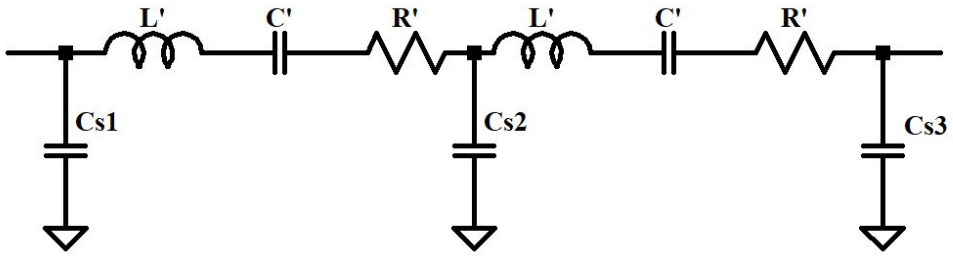

Figure 2.10 Equivalent circuit of IDC at high frequency.

R' is the series resistance defined as

$$R' = 1.33\frac{l}{WN}R_s \tag{2.51}$$

where R_s is the sheet resistivity. The capacitance C_s and inductance L can be derived using transmission line theory as

$$C_s = 0.5 \times \frac{\sqrt{\varepsilon_{re}}}{Z_0 c}l \tag{2.52}$$

$$L = \frac{Z_0\sqrt{\varepsilon_{re}}}{c}l \tag{2.53}$$

where c is the light speed in the vacuum, Z_0 and ε_{re} are the characteristic impedance and effective dielectric constant respectively. The approximation expression for the total capac-

itance of an interdigital capacitor at high frequency can be described as

$$C = \frac{\varepsilon_{re} l}{18\pi} \times \frac{K(k)}{K'(k)} (N-1) \times 10^{-3} (pF), \tag{2.54}$$

where $k = tan^2\left(\frac{W\pi}{4(W+S)}\right)$,$k' = \sqrt{1-k^2}$, $\frac{K(k)}{K'(k)} = \frac{1}{\pi} ln(\frac{2(1+\sqrt{k})}{1-\sqrt{k}})$ for $\frac{1}{\sqrt{2}} \leq k \leq 1$ and $\frac{K(k)}{K'(k)} = \frac{\pi}{ln(\frac{2(1+\sqrt{k\prime})}{1-\sqrt{k\prime}})}$ for $0 \leq k \leq \frac{1}{\sqrt{2}}$.

In practice, due to the complexity of equations, it is more practical to simulate the capacitance of IDC in high-frequency domain using CAD software like HFSS. The design process and optimization will be discussed in detail in the later chapter.

Chapter 3

Ion Sensitive Electrode Design

3.1 Ion-selective membrane solution Preparation

A typical ISE is usually composed of a reference electrode and a sensing electrode for specific ion monitoring. The performance of the sensing electrode is mainly determined by the ion-selective membrane coated. It is important to prepare a suitable ion-selective membrane for the particular ISE application. The membrane solution is normally composed of ionophores, ion exchangers, plasticizers, polymers matrixes, and solvents.

The ionophores are tiny, lipid-soluble molecules that convey target ions to pass through the membrane. They act as membrane shuttles for corresponding ions to travel through the membrane down their electrochemical gradient without the expenditure of energy. Different ions have their own corresponding ionophores. In this thesis, potassium ion is our interest. Valinomycin is chosen as the potassium selective ionophore for its outstanding potassium ion transport rate. It can transport around 10000 K^+ ions per second per molecule through the cell membrane due to the puckered rings in its structure [59].

The ion exchangers are lipophilic salts that can exchange cations or anions or even both. It supports the establishment of membrane interface charge confinement. Potassium tetrakis (4-chlorophenyl) borate is selected as ion exchangers in this thesis. Doping with Valinomycin

(ionophore), the K^+ selectivity of the membrane solution is primarily determined. Compared with the ionophores, the hydrophilic ions dissociated from the ion exchangers can cross the membrane interface freely without covalently bonding to the polymeric matrix of the membrane. Ion exchangers improve the overall performance and stability of the membrane significantly.

Polymeric matrixes are designed to enhance the membrane's mechanical stability and resistance to external pressure. They are usually soft and rubbery amorphous materials such as Polyvinyl chloride (PVC), having a high degree of mobility of polymer chains, which allows good adhesion between the polymer and inorganic matrix. They can provide rubber-like homogenous hydrophobic medium to ionophore complexes to move freely without interfering with the membrane structure. As the result, an interfacial void-free membrane could be easily achieved. PVC is selected as the polymeric matrix material in this thesis.

Platisicers are usually used for plastic membranes as additives that enhance the membrane's flexibility and stability. The plasticizers embed themselves between the chains of the polymer to space them apart to increase the free volume [60]. The more the added plasticizer, the more flexibility, better durability, and lower cold flex temperature can be achieved. Platisicers might be ethers, esters of either aromatic or aliphatic acids. In our case, Bis (2-ethylhexyl) sebacate behaves as the plasticizing solvent mediator in the prepared membrane for better elasticity and ionophore solubility.

The final configured potassium ion-selective membrane solution consists of 4 mg of valinomycin, 1 mg of Potassium tetrakis(4-chlorophenyl)borate, 129.4 mg Bis (2-ethylhexyl) sebacate, 65.6 mg of PVC as well as 2 ml tetrahydrofuran (THF) as solvent.

3.2 K^+ ion sensitive Electrode

3.2.1 Design and Fabrication

The layout of the proposed potassium ion-selective electrode is shown in Figure 3.1. The sensing electrode has a circular detection area of 5 mm radius coated with the configured potassium ion selective membrane solution, while the reference electrode maintained a constant distance of 9 mm away from the sensing electrode.

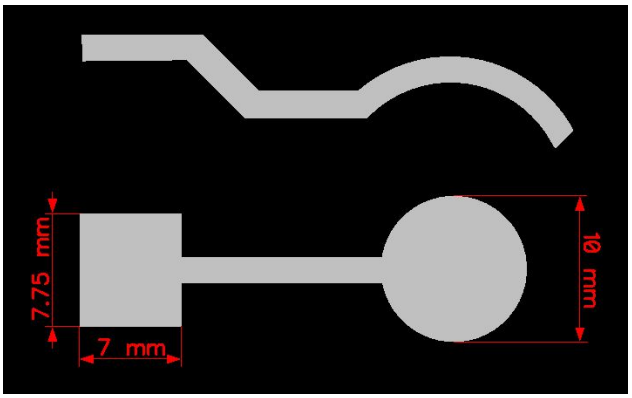

Figure 3.1 Layout of proposed ISE (top is for reference and bottom is for sensing electrodes, respectively)

A Voltera inkjet printer is used for designed ISE layout printing. It supports DOD mode and a minimum resolution size of 200 μm. The average deposition thickness is 50 μm. A 127 mm thickness Dupton Kapton polyimide (PI) film is selected as substrate material for its excellent dielectric constant. The resistivity of the flexible silver nanoparticle conductive ink is small ($\rho = 1.36 \times 10^{-7} \Omega \bullet m$). After the layout is printed, casting the configured ion selective membrane solution on the circular detection area of the sensing electrode followed by an evaporation period of more than 24 hours are performed. Afterward, soaking the ISE into 1M KCl solution for at least 12 hours to establish a steady-state is done. Eventually, two jumping wires are connected to the terminals of the electrodes via conductive epoxy for capacitance-resistance measurement. The printed proposed ISE is shown in Figure 3.2.

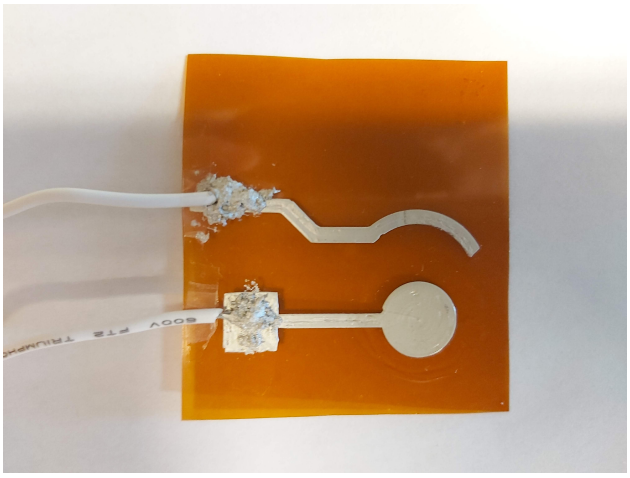

Figure 3.2 Printed proposed ISE

3.2.2 ISE Measurement

Before ISE measurement, a couple of testing solutions with different K^+ concentrations needs to be prepared. Potassium chloride (KCl) solutions with varying K^+ molarities between 0.001 mol/L to 2 mol/L are made at room temperature. As shown in Figure 3.3, the parallel capacitance and parallel resistance developed across the electrodes are measured with an LCR meter for each of these KCl solutions at 20 MHz. In between two measurements, the ISE was cleaned with DI water and dries with kimwipes.

Figure 3.3 Measurement set up with prototype K^+ ISE

The measured capacitance across the ISE at the room temperature (20°C) is plotted in Figure 3.4. for K^+ concentration over 0.001 to 2 mol/L K^+ concentration. It shows a 2nd order exponential relationship between different K^+ molarities and measured capacitance as shown in Fig. 4. The exponential fit is given by

$$f(x) = 318 \times e^{0.03x} - 317.2 \times e^{-12.81x} \tag{3.1}$$

where $f(x)$ and x represent $C(K+)$ and K^+ molarity respectively over the 0.001-2mole/L K^+ dynamic range. For all measurements, a minimum of 6.547 pF was observed at 0.001 mole/L. Afterward, the capacitance surges very quickly until about 300 pF at 0.5mol/L. Then the capacitance value slowly increases from 0.5 mole/L to 2 mole/L. It can be seen that with higher K^+ molarity, the capacitance increases in the presence of valinomycin, indicating that more K^+ ions are translocated across the membrane. Similar trends were observed by Su et al. in [61].

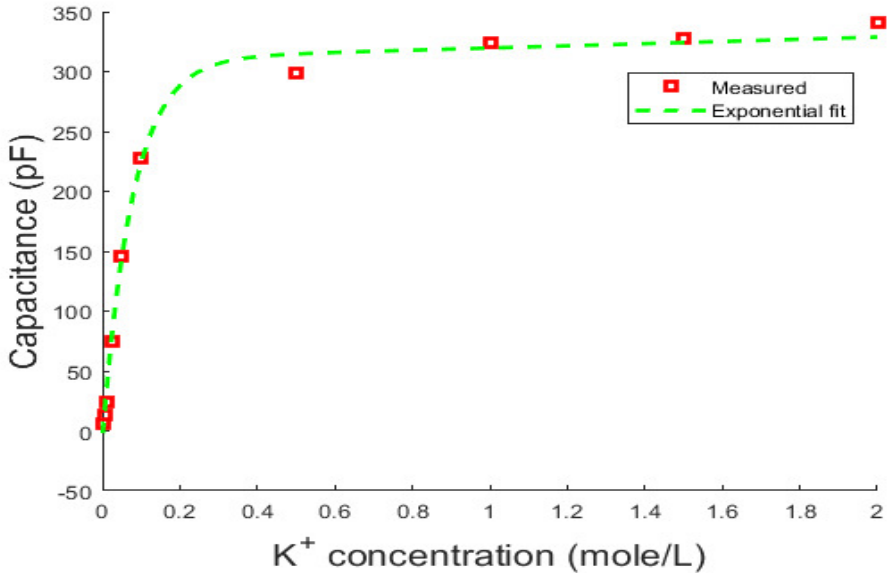

Figure 3.4 Capacitance across ISE for different K^+ concentration

For K^+ selective electrodes using valinomycin as ionophores, the membrane resistance

depends on the morphology of the electrode, concentration, and type of plasticizers [61, 62]. Figure 3.5 shows the resistances measured across the ISE for different K^+ concentrations. In contrast to the capacitance, the maximum resistance was 10.774 kΩ at 0.001 mole/L. Afterward, the resistance would plump to a minimum of 0.6 kΩ at 0.05 mole/L. Then the resistance value maintained a constant level of around 1.5 kΩ from 0.5 mole/L to 2mole/L. From the change of resistance values, it is evident that the quality factor of the RFID sensor incorporated with the proposed ISE will not decrease monotonically as K^+ increases. It is difficult to derive the correct K^+ molarity based on the quality factor as the calculated quality factor value turned out to be low for molarity 0.1 to 2 mol/L. So the quality factor of the RFID sensor based on the proposed ISE is not a suitable parameter for K^+ detection in practice. Therefore, the resonant frequency is chosen as a reliable tracking parameter for K^+ molarity detection in the later RFID sensor design that is incorporated with the proposed ISE.

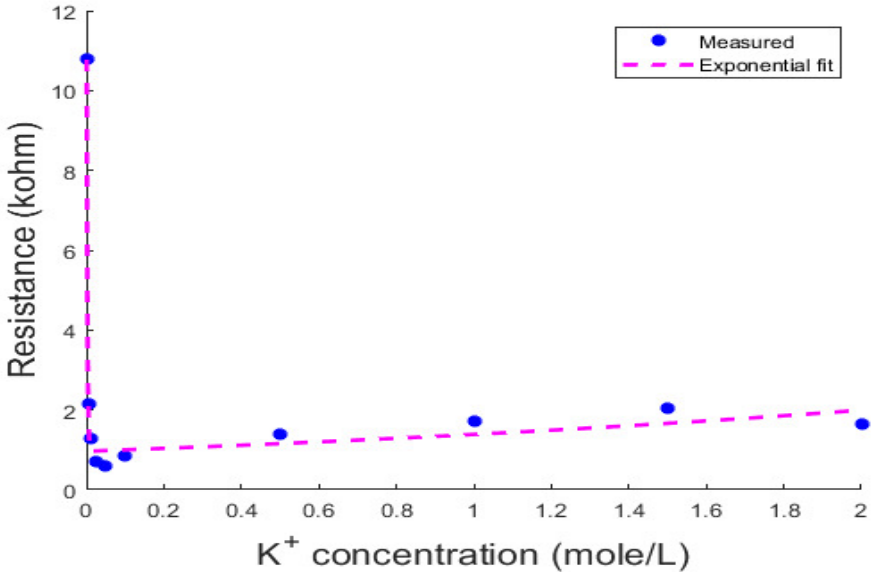

Figure 3.5 Resistance across ISE for different K^+ concentration

Chapter 4

Printer LC Resonator and Interrogator Design

4.1 LC Resonator based on PCB Substrate

4.1.1 Design and Simulation

The geometrical layout of the proposed LC resonator on PCB Substrate is shown in Figure 4.1. The LC resonator is designed to resonate around 20 MHz. It consists of a square spiral inductor and an interdigital capacitor. The resonator is designed to print on a 1.5 mm thick FR4 Epoxy (ε_r = 4.4, tanδ = 0.02) board using the Voltera inkjet printer using the same type of flexible conductive ink mentioned before.

As shown in Figure 4.1, for the proposed square spiral inductor, number of turns n = 7, the turn width w = 0.5 mm, turn spacing s = 0.6 mm, inner diameter d_{in} = 46.8 mm and outer diameter d_{out} = 61 mm. The thickness of the conductive segments is 50 μm, which is relatively small and has few effects on inductance. As the spiral inductor consists of many turns of conductive segments, the self-indutive and mutual-inductive effects in each segment will cause phase shift leading to the impressed conductive current. Meanwhile, the

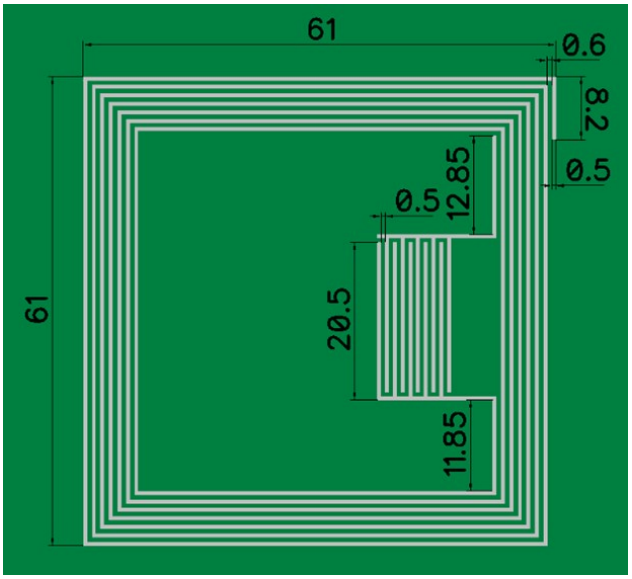

Figure 4.1 Dimension of proposed LC resonator design on PCB substrate.

presence of the substrate and closely spaced segments will cause the accumulation and flow of charge at the surface of the substrate and neighboring segments. It is hard to describe the inductance of the spiral inductor in an accurate and straight expression. To solve this problem, significant work has gone into modeling the approximate inductance using simple expressions. For example, Mohan et al. [50] approximation as following

$$L_{square} = \frac{n^2 d_{avg} c_1 \mu_0}{2} \left[ln(\frac{c_2}{\rho}) + c_3 \rho + c_4 \rho^2 \right] \tag{4.1}$$

where the layout-dependent coefficients $c_1 = 1.27$, $c_2 = 2.07$, $c_3 = 0.18$, and $c_4 = 0.13$ respectively. However, the calculated inductance deviates from the actual value due to the loss of the substrate in practice. Since the induced substrate charge would flow through the lossy substrate. A more accurate inductance value can be calculated by solving Maxwell's equation using High-Frequency Structure (HFSS) simulator. The accurate inductance of the spiral inductor can be derived using the imaginary impedance Z11 via the formula $L = \frac{im(Z11)}{2\pi f} \times 10^6(\mu H)$. The plot of the corresponding frequency-dependent inductance of the spiral inductor is shown in Figure 4.2. An inductance of 11.36 μH is obtained at 20 MHz.

It is noticed that the inductor has a self-resonance frequency of around 29.7 MHz due to its parasitic capacitance.

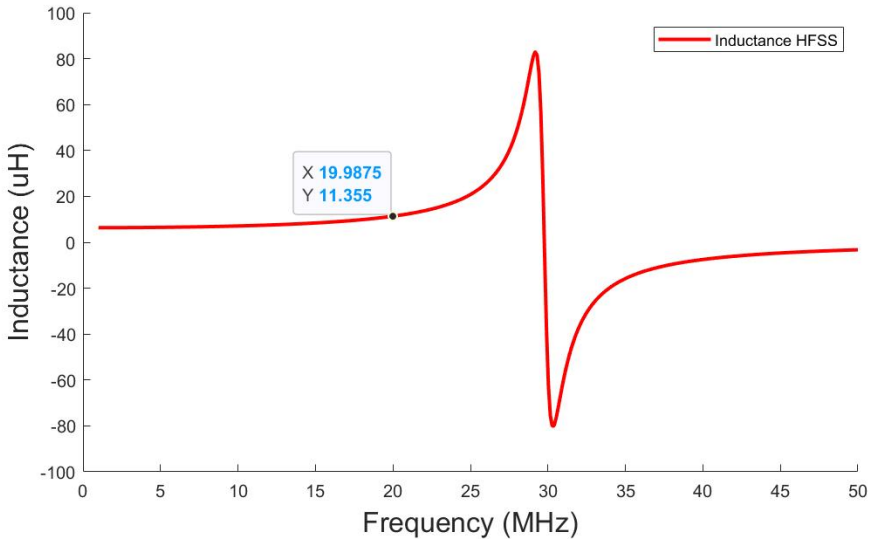

Figure 4.2 Frequency-dependent Inductance simulation on PCB substrate.

Referring to Figure 4.1, an interdigital capacitor with a multi-finger structure was connected to the spiral inductor. Capacitance occurs across the narrow gap between neighboring fingers. In order to obtain a 20 MHz resonant frequency, the matched capacitor was derived as 5.57 pF using equation $f = \frac{1}{(2\pi\sqrt{LC})}$ and the simulated inductor value. However, this capacitance does not take the parasitic capacitance into account. It is necessary to tune the capacitance so that the tag could resonate at 20 MHz. For the proposed interdigital capacitor shown in Figure 4.1, the finger width w = 0.5 mm, finger spacing s = 0.5 mm, finger length l = 20.5 mm, and the number of fingers N = 10. The finger width and space width is designed to be equal for maximum capacitance density. Similar to the calculation of inductance, the accurate capacitance could be calculated exactly by Maxwell's equations using the HFSS simulator too. The accurate capacitance can be derived using the imaginary Z11 via the formula $C = \frac{-1}{im(Z11)\times 2\pi f} \times 10^{12}$ (pF). The corresponding frequency-dependent capacitance of the interdigital capacitor is shown in Figure 4.3. A capacitance of 9.67 pF is

computed at 20 MHz.

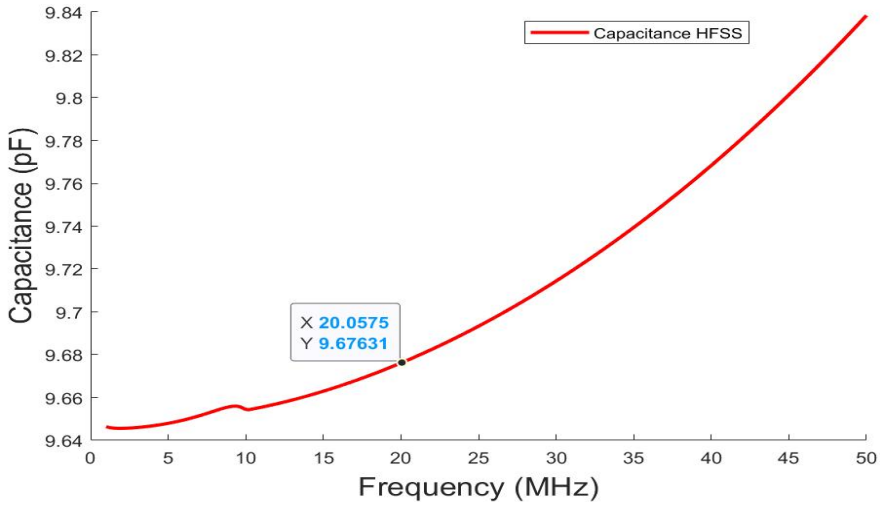

Figure 4.3 Frequency-dependent capacitance simulation on PCB substrate.

Connecting the spiral inductor and interdigital capacitor in the HFSS simulator and then measure the Z11 value between the two terminals. We could get the simulation result shown in Figure 4.4, both maximum real Z11 and zero imaginary Z11 suggested that the entire LC resonator has a resonance around 20 MHz. This simulation result meets the design target based on the wired simulation result.

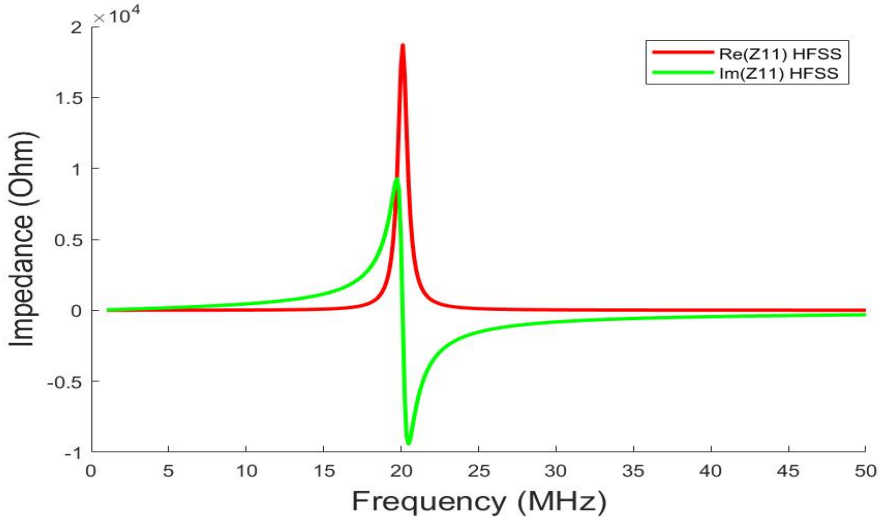

Figure 4.4 Z11 simulation of LC resonator on PCB board.

Moving on to the wireless simulation, an experimental setup including coupled interrogator coil and LC resonator was modeled in HFSS as shown in Figure 4.5. Noted that the interrogator coil was aligned concentrically with the printed inductor. The details of the coil interrogator will be introduced in a later subsection. The S11 parameter at the interrogator coil with regards to the distance d = 2 cm between interrogator and resonator was simulated as shown in Figure 4.6. The distance should not be smaller than 2 cm to avoid the over coupling effect. According to Figure 4.6, the wireless simulation demonstrates that the resonant frequency of the LC resonator is almost 20 MHz, which matches well with the simulated resonant frequency obtained from the wired HFSS simulation.

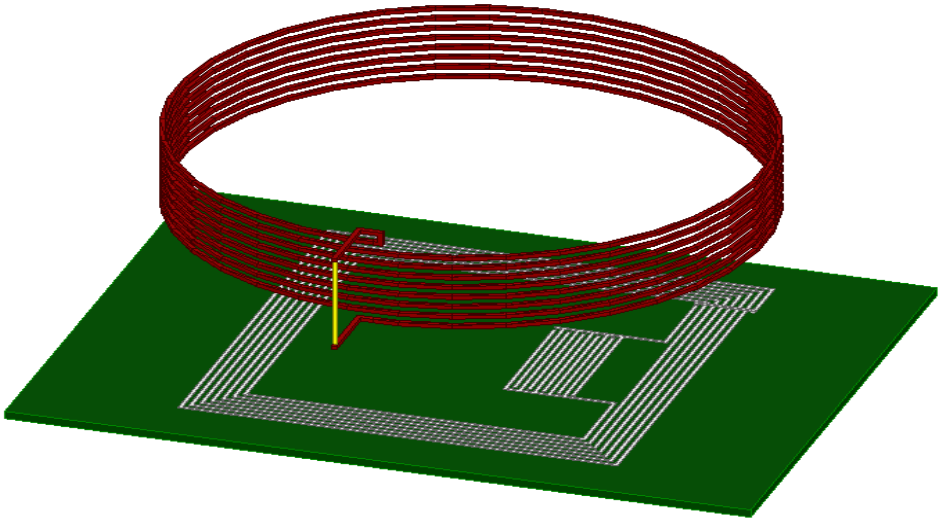

Figure 4.5 Experimental setup with coupled interrogator coil and LC resonator on PCB substrate in HFSS.

4.1.2 Varying distance measurement

The proposed LC resonator layout is printed using an inkjet printer from Voltera using the same conductive ink and baked in an oven to remove dispersants in ink. The printed prototype is shown in Figure 4.7. Since the printer could not print out the conductive air bridge in practice, an extra jumping wire and some conductive epoxy are added to connect

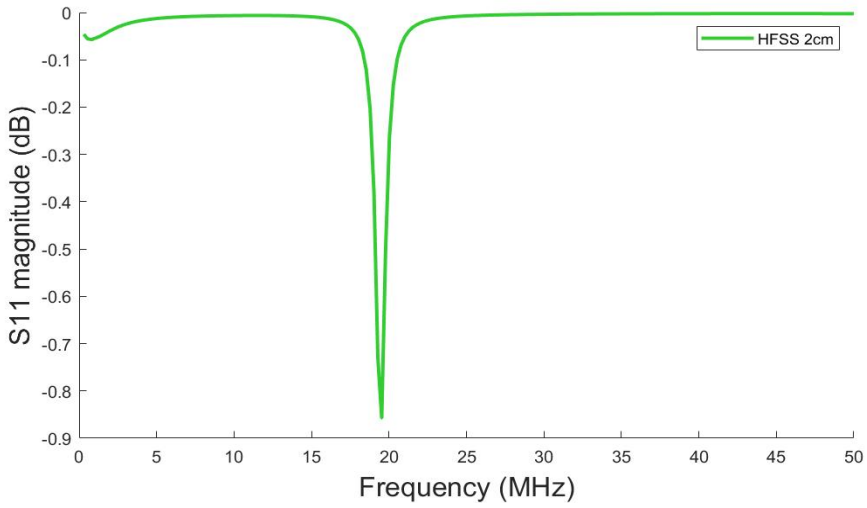

Figure 4.6 Simulated S11 for LC resonator on PCB substrate.

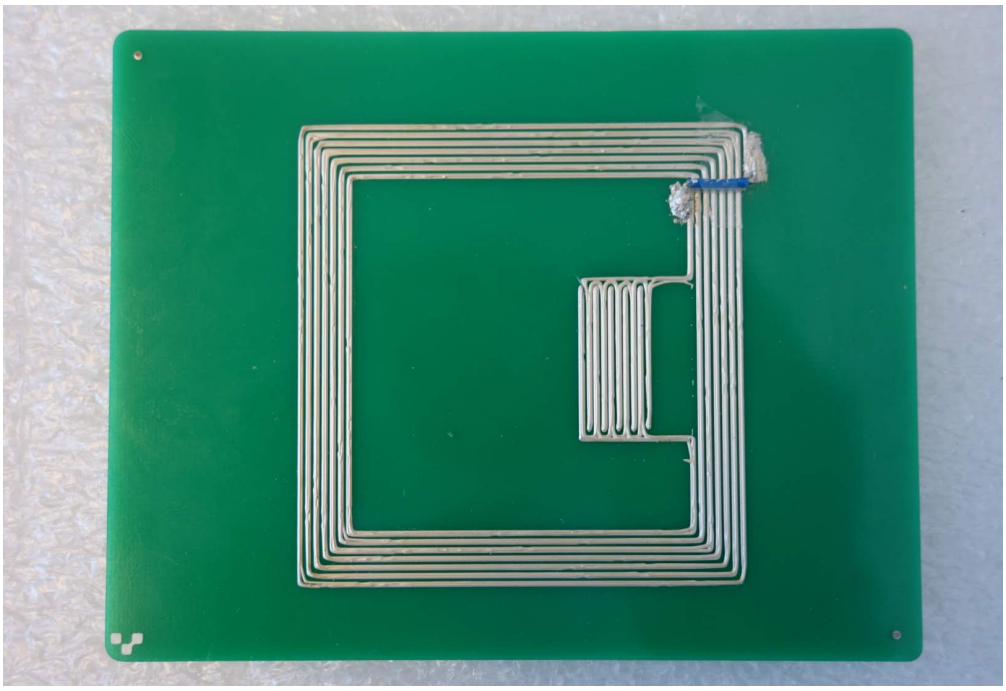

Figure 4.7 Printed prototype LC resonator on PCB board.

two terminals of the printed RFID tag. Then, a copper interrogator coil is placed in front of the RFID tag as shown in Figure 4.8. A vector network analyzer (VNA) is connected to the interrogator coil via an SMA connector. The measured S11 parameter at the interrogator coil is plotted in Figure 4.9. From the plot, the measured S11 response matches well with

the HFSS simulation. The resonant frequency of the RFID tag prototype is measured to be around 20.5MHz. The small deviation between the simulation and measurement was mainly due to the parasitic capacitance caused by jumping wires and conductive epoxy. The increase of the quality factor of the measured resonances is mainly contributed by the dimension distortion during printing and the thickness uniformity issue of the printed layer. From the valley of each S11 trial with a step size of 1 cm, it is evident that the magnitude of the magnetic field drops as $\frac{1}{R^6}$, where R is the distance between interrogator and tag.

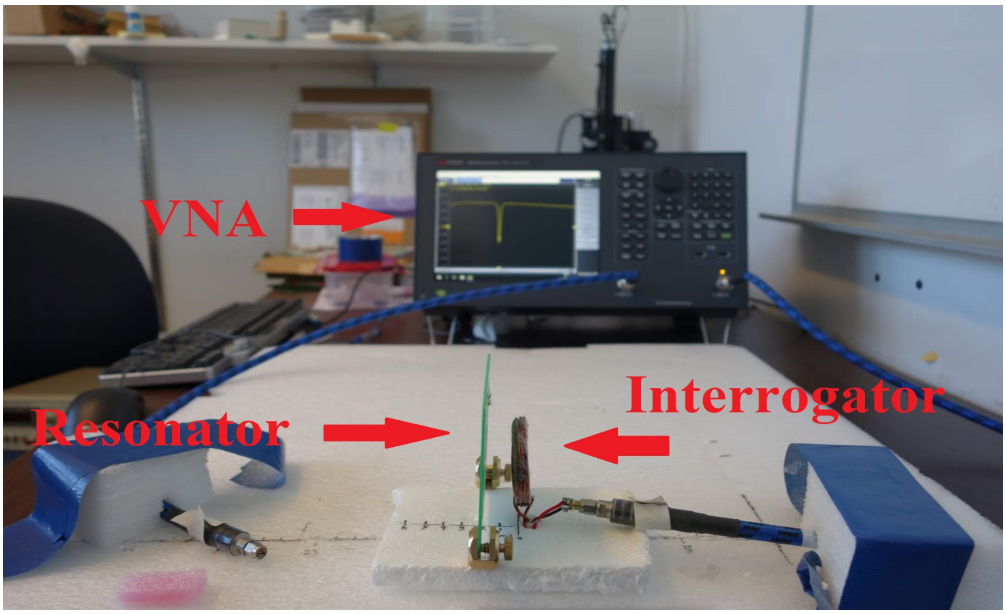

Figure 4.8 S11 measurement setup for LC resonator on PCB board.

4.2 LC Resonator based on Kapton Substrate

4.2.1 Design and Simulation

The geometrical layout of the proposed LC resonator on Kapton Substrate is shown in Figure 4.10. The designed resonant frequency is also 20 MHz. The LC resonator is composed of a square spiral inductor and an interdigital capacitor. It will be printed on a 127 mm thick Kapton polyimide film using the Voltera inkjet printer using the same flexible conductive

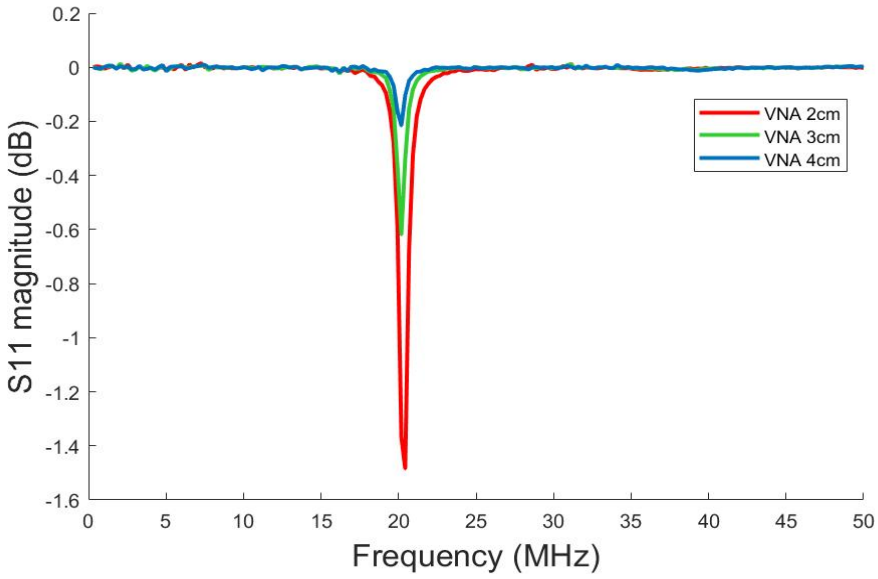

Figure 4.9 Measured S11 parameter at interrogator for LC resonator on PCB board.

ink.

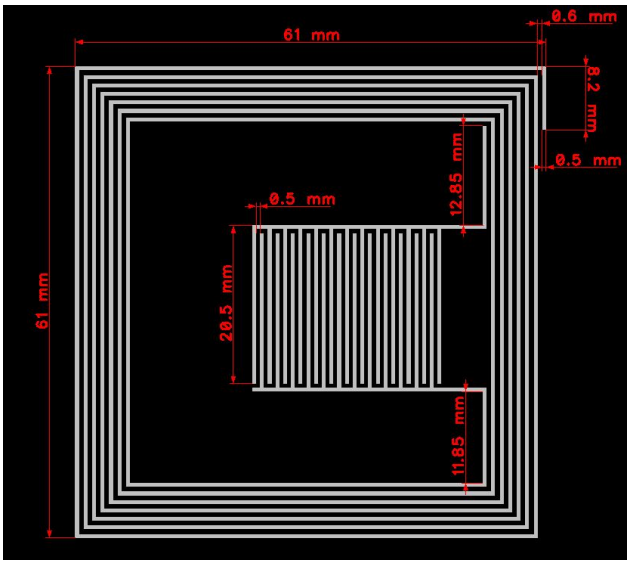

Figure 4.10 Dimension of proposed LC resonator design on Kapton substrate.

As shown in Figure 4.10, the proposed square spiral inductor has the same physical parameters as the previous inductor design: number of turns n = 7, the turn width w = 0.5 mm, turn spacing s = 0.6 mm, inner diameter d_{in} = 46.8 mm and outer diameter d_{out}

= 61mm. However, due to the changed dielectric constant of the substrate, its inductance varies accordingly. An accurate inductance value can also be calculated by solving Maxwell's equation using High-Frequency Structure (HFSS) simulator. The plot of the corresponding frequency-dependent inductance of the spiral inductor is shown in Figure 4.11. An inductance of 11.54 μH is obtained at 20 MHz.

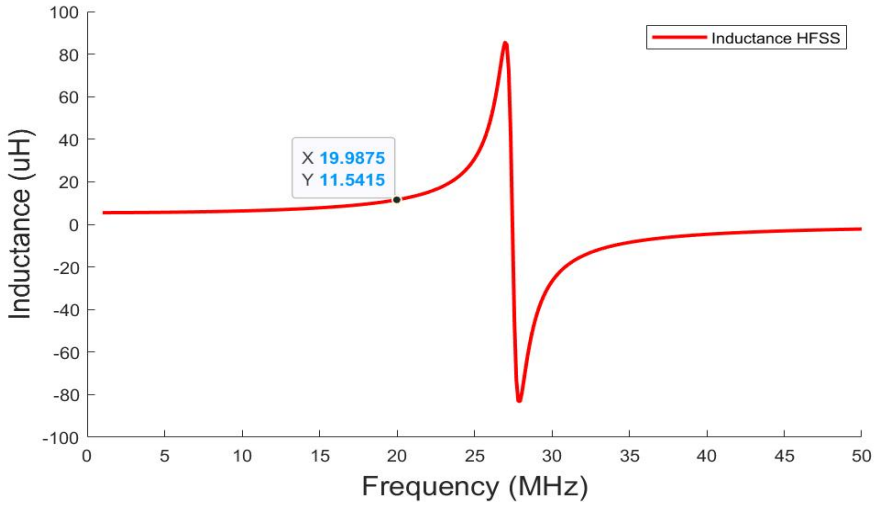

Figure 4.11 Frequency-dependent inductance simulation on Kapton substrate.

For the proposed interdigital capacitor shown in 4.10, the finger width w = 0.5 mm, finger spacing s = 0.5 mm, finger length l = 20.5 mm, and the number of fingers N = 25. Similar to the calculation of inductance, the accurate capacitance could be calculated accurately by Maxwell's equations using the HFSS simulator via the imaginary Z11. The corresponding frequency-dependent capacitance of the interdigital capacitor is shown in Figure 4.12. A capacitance of 49.2 pF is achieved at 20 MHz.

Again, connecting the spiral inductor and interdigital capacitor in the HFSS simulator and then measure the Z11 value between the two terminals. We could get the wired simulation result shown in Figure 4.13, both maximum real Z11 and zero imaginary Z11 illustrated that the proposed LC resonator has a resonant frequency of 20 MHz.

For the wireless simulation, an experimental setup including coupled interrogator coil

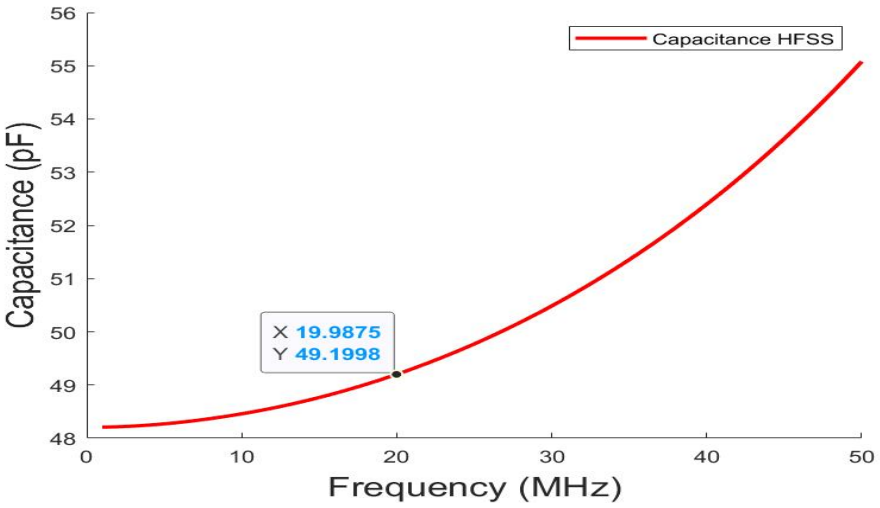

Figure 4.12 Frequency-dependent capacitance simulation on Kapton substrate.

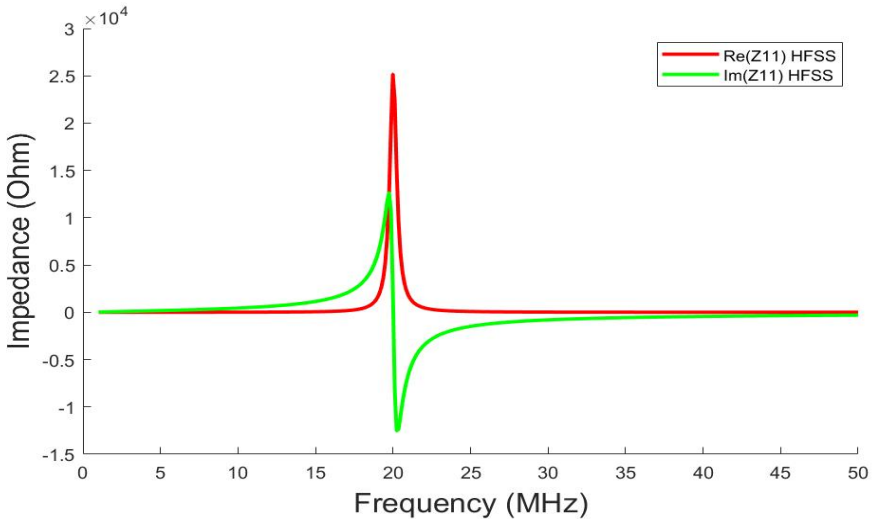

Figure 4.13 Simulated Z11 of LC resonator on Kapton substrate.

and LC resonator was modeled in HFSS as shown in Figure 4.14. The S11 parameter at the interrogator coil with a distance of d = 2 cm between the interrogator and the resonator was simulated as shown in Figure 4.15. The simulated S11 plot demonstrates that the resonant frequency of the proposed LC resonator on Kapton film is closed to 20 MHz, which matches well with the simulated resonant frequency obtained from the wired HFSS simulation.

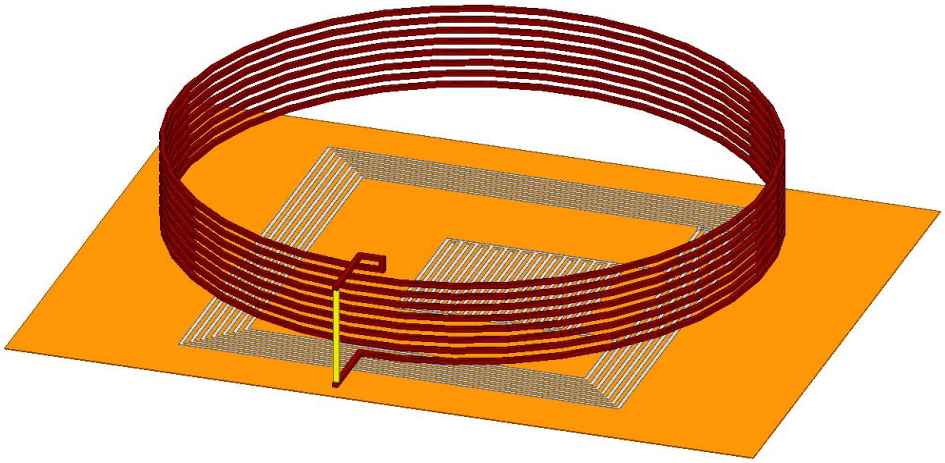

Figure 4.14 Experimental setup with coupled interrogator coil and LC resonator on Kapton substrate in HFSS.

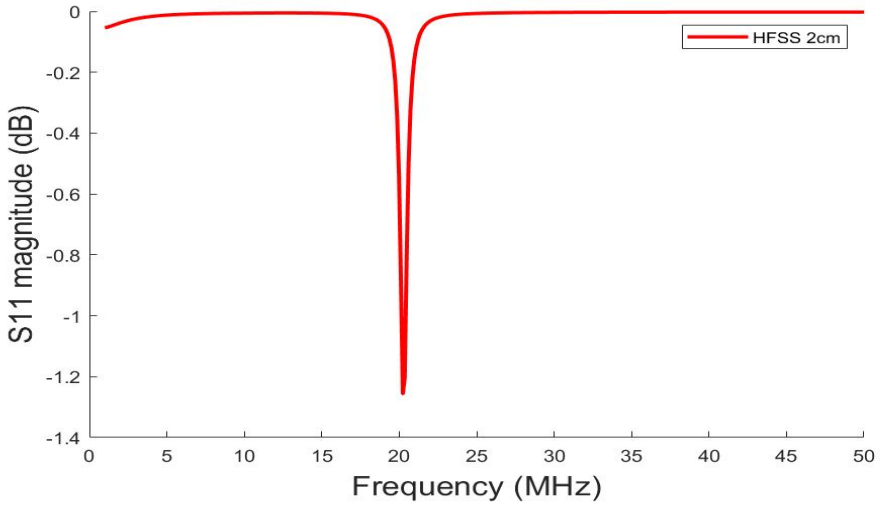

Figure 4.15 Simulated S11 for LC resonator on Kapton substrate.

4.2.2 Varying distance measurement

The proposed LC resonator layout is printed on Kapton film using the same inkjet printer from Voltera and baked in an oven to remove dispersants in ink. The printed LC resonator prototype is shown in Figure 4.16. A jumping wire will be added to connect the terminals.

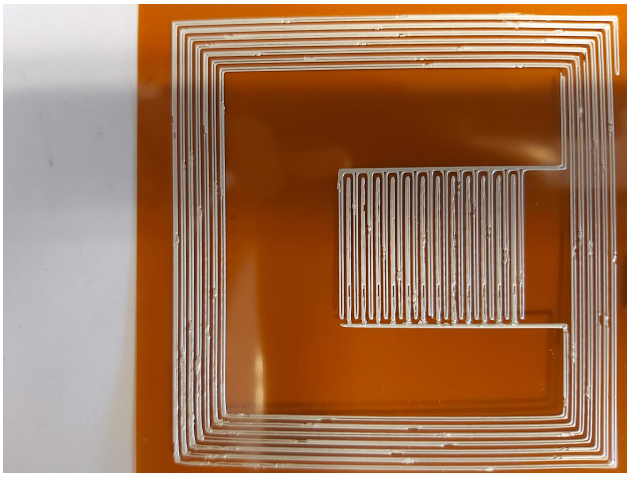

Figure 4.16 Printed prototype LC resonator on Kapton film.

A copper interrogator coil connected to the VNA is placed in front of the RFID tag as shown in Figure 4.17. The measured S11 parameter at the interrogator coil is plotted in Figure 4.18. From the plot, the measured S11 response matches well with the HFSS simulation. The resonant frequency of the RFID tag prototype is measured to be 19.97 MHz. It meets the requirement of target resonant frequency.

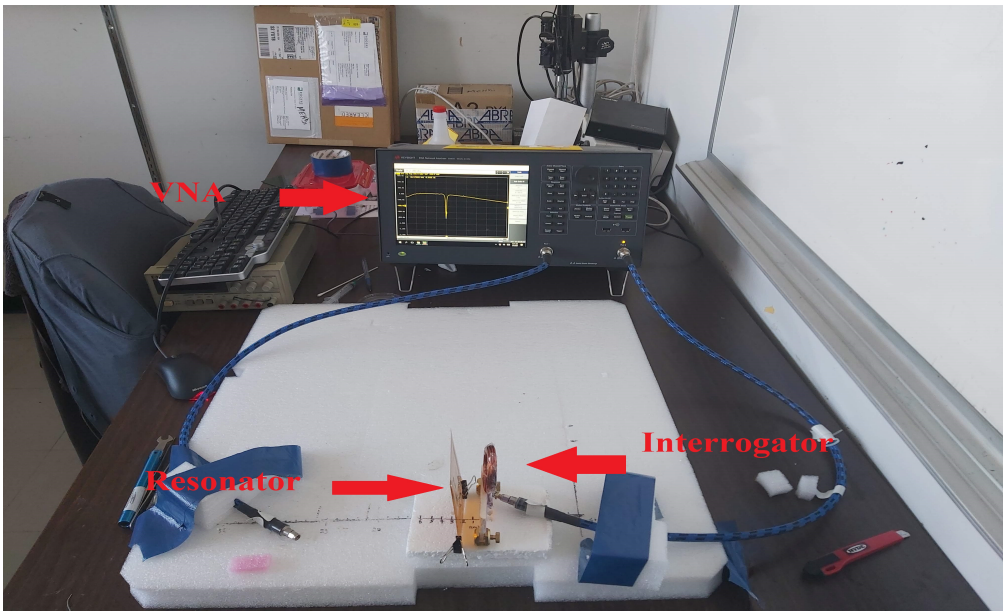

Figure 4.17 S11 measurement setup for LC resonator on Kapton film.

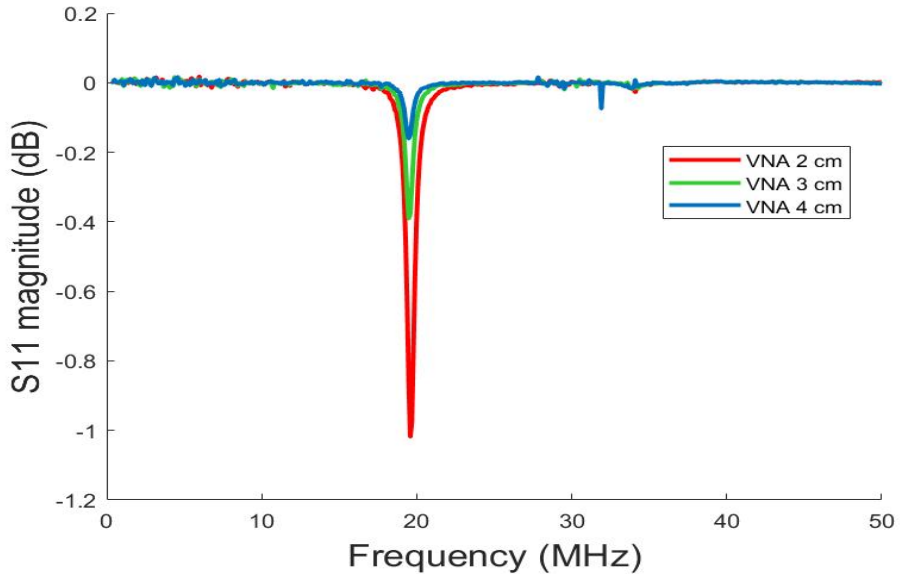

Figure 4.18 Measured S11 parameter at interrogator for LC resonator on Kapton film.

4.3 Interrogator Coil

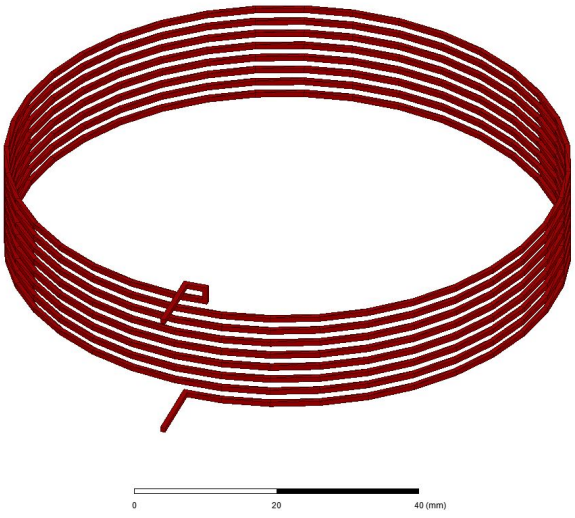

Figure 4.19 Proposed interrogator coil.

The cylindrical solenoidal coil interrogator is characterized by its number of turns N, length of solenoid l, pitch p, and loop radius R. The designed interrogator coil has 8 turns

of insulated copper wire of 1 mm diameter, a pitch of 2 mm, a solenoid length of 16 mm, and a radius of 40 mm as plotted in Figure 4.19. The total magnetic flux through the coil is given as

$$\Phi = \mu \frac{NIA}{l} \tag{4.2}$$

where μ is the magnetic permeability of the outside environment, I is the current within the coil, and A is the cross-section area. The corresponding inductance in the low-frequency domain can be calculated by

$$L_{interrogator} = \frac{N\Phi}{I} = \frac{\mu N^2 A}{l}. \tag{4.3}$$

Moreover, in the high-frequency domain, the coil acts as an oscillatory tank circuit with an inductor and capacitor in parallel [63]. It has a resonant frequency given by

$$f_r = \frac{1}{2\pi\sqrt{LC}} \approx \frac{1}{2\pi\sqrt{LC_T}} \tag{4.4}$$

where C_T is the capacitance of the variable tuning capacitor (approximately equal since stray capacitance and self-capacitance of the coil are being neglected) and L is coil inductance. A good estimator of the self-inductance of a solenoidal coil was derived by Niwa [64]. However, that formula contains a summation of 12 terms based on the coil geometry and is inconvenient to calculate in practice. Therefore, an HFSS model of the designed copper coil is made and simulated to find out its self-inductance and self-resonant frequency. The variation of the inductance against frequency for the coil interrogator is illustrated in Fig. 2. Based on the simulation, the inductance is around 11.07 μH at 20 MHz. It is closed to the value of the printed planar spiral inductor. Meanwhile, it has a self-resonant frequency of 37.44 MHz which is far enough from the LC resonator's resonant frequency.

Chapter 5

Flexible Printed Inductive-Capacitive Resonator based RFID Sensor for remote K^+ Ions Detection

5.1 Flexible Printed Chipless RFID Sensor

5.1.1 Printed Prototype Design

The proposed flexible printed RFID tag is the combination of the LC resonator and the K^+ ISE presented in the previous chapter. The printed prototype RFID tag is shown in Figure 5.1. The tag is printed on a 127mm thick Kapton film by a Voltera printer. As the printer could not print out the conductive air bridge in practice, a couple of jumping wires and some conductive epoxy were added to connect the LC resonator and the K^+ ISE in parallel. The tag can keep track of the K^+ concentration based on the fact that the capacitance developed across the ISE varies with the change of K^+ in the solution displayed in chapter 3. The operating frequency of the RFID tag is around 20 MHz and thus belongs to the HF RFID system.

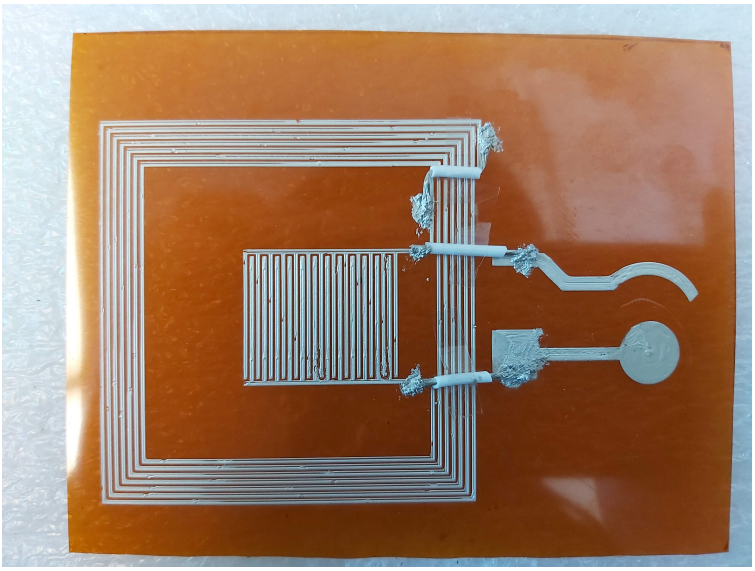

Figure 5.1 RFID tag printed for K^+ sensing.

5.1.2 Working Principle

Before moving on to the measurement process, it is necessary to explain the working principle of the entire proposed RFID system for remote K^+ sensing. A block diagram of the inductively coupled interrogator and RFID tag is shown in Figure 5.2. Here, L_1 represents the inductance of the interrogator coil while L_S is the inductance of the printed inductor and C_p indicates the fixed capacitance of the printed interdigital capacitor in the RFID tag. $C(K^+)$ is the capacitance developed at the ISE when in contact with a solution. The capacitance, $C(K^+)$ changes in response to the K^+ concentration change in the solution. The RFID inductor and total capacitor, $C_{total} = C_p + C(K^+)$ form a resonant circuit with a resonant frequency f_r approximately given by

$$f_r = \frac{1}{2\pi\sqrt{L_s \times C_{total}}} \tag{5.1}$$

Inductive coupling based on Faraday's law of magnetic induction is the key mechanism behind this HF RFID system. The printed inductor of the RFID tag is inductively coupled to

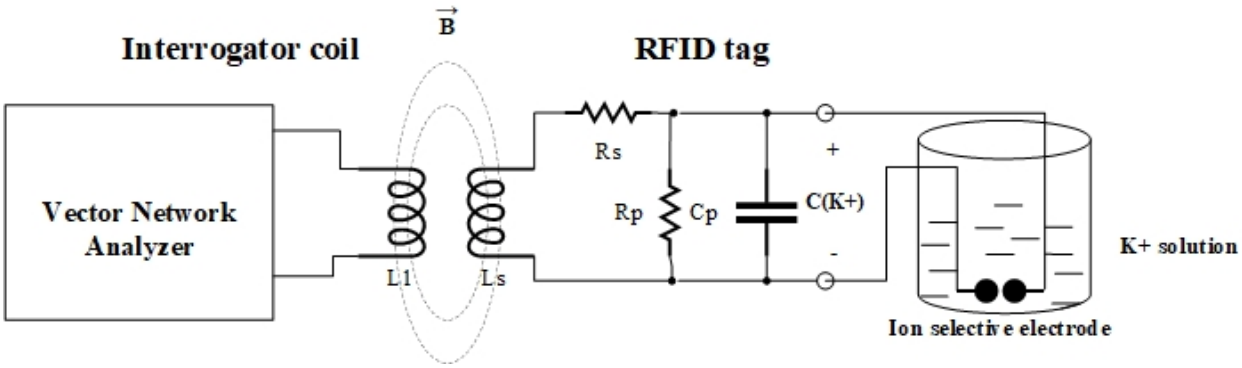

Figure 5.2 Block diagram of the coupled coil interrogator and RFID tag.

the interrogator coil, whose reflection coefficient (S11) is monitored using a swept frequency VNA. The resonant frequency of the weakly coupled RFID tag is measured by measuring the perturbation of interrogator coil S11 response. Since the resonant frequency of the RFID tag is directly related to the capacitance across the ISE, the K^+ concentration in the liquid can be measured from the S11 response measured at the interrogator coil when coupled to the tag.

An equivalent circuit diagram of the coupled RFID tag is shown in Figure 5.3. In this circuit, R_1 and L_1 represent the series resistance and inductance of the interrogator coil, respectively. L_s and R_s are the series inductance and resistance of the inductor of the LC resonator part, respectively. C_p and R_p are the capacitance and resistance of the fixed capacitor of the LC resonator part, respectively. Noted that the series resistance of the inductor is a very small resistance as the ink used for printing is mainly made of silver. $C(K^+)$ and $R(K^+)$ are the junction capacitance and resistance developed at high frequency across the ion-selective electrodes when in contact with a K^+ solution. As the concentration of the potassium ion changes, the $C(K^+)$ changes quickly and dominates the total equivalent capacitance and resonant frequencies of the RFID sensor. M is the interrogator-RFID coil coupling factor. For small M and low circuit losses, the concentration of K^+ in the analyte solution, which is indicated by $C(K^+)$, can be monitored by tracking the resonant frequency

of the RFID sensor.

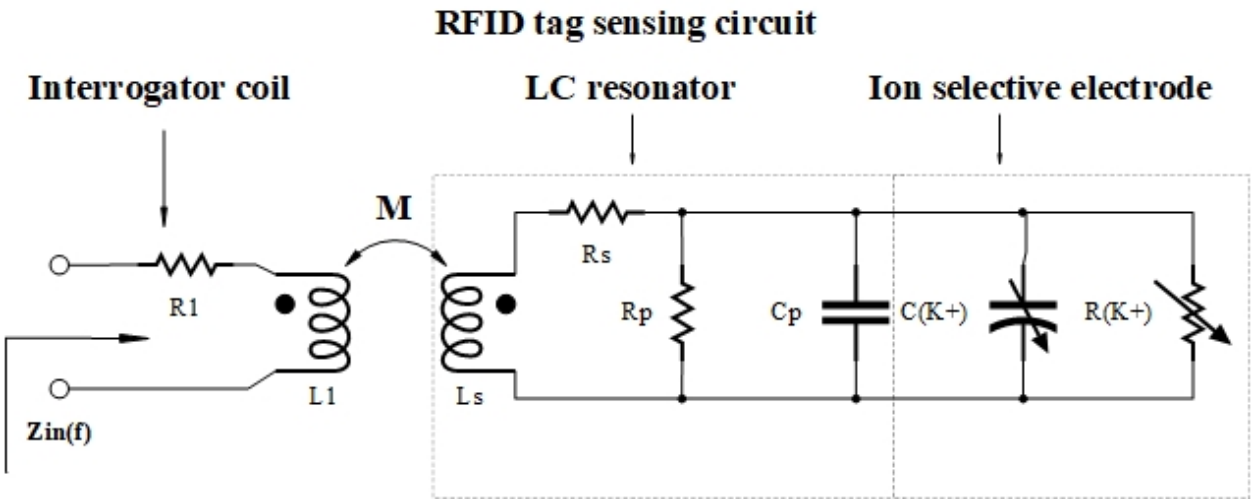

Figure 5.3 Equivalent circuit diagram of the RFID sensor.

Based on Figure 5.3, the LC resonator is in parallel with the ISE, thus the resonant frequency f_r of the RFID tag is given as $f_r = \frac{1}{2\pi\sqrt{L_s \times C_{total}}}$, where $C_{total} = C_p + C(K^+)$ is the total capacitance in parallel with the printed inductor. The input impedance, $Z_{in}(f)$, seen by the vector network is

$$Z_{in}(f) = Z_1 + Z_T = R_1 + j2\pi f L_1 + \frac{(2\pi f)^2 M^2}{Z_{total}} \tag{5.2}$$

where f is the source frequency and $Z_{total} \approx j2\pi f L_s + R_s + 1/[(1/R_p + 1/R(K^+)) + j2\pi f(\ C_p + C(K^+))]$ is the RFID series impedance. The input impedance $Z_{in}\,(f)$ contains two main components; $Z_1 = R_1 + j2\pi f L_1$, due to self impedance of the interrogator coil and $Z_T = \frac{(2\pi f)^2 M^2}{Z_{total}}$, due to RFID coupling. When the interrogator coil is connected to a VNA, reflection occurs between the VNA source impedance and the interrogator coil input impedance. The reflection coefficient (S11) measured by the VNA is given by

$$S_{11} = \frac{Z_{in} - Z_{source}}{Z_{in} + Z_{source}} \tag{5.3}$$

where Z_{source} is the source impedance of the VNA driver and Z_{in} is the above input impedance. At the resonant frequency f_r of the RFID sensor, the parallel impedance Z_{total} is at its peak and therefore Z_{in} and S11 is at its minimum respectively. To remove the effect of the background noise from the interrogator, a background subtraction using the measured S11 of coil interrogator when the RFID tag is absent, should be implemented after measuring the RFID sensor response.

5.2 S11 and f_r Measurement for varying K^+ concentration

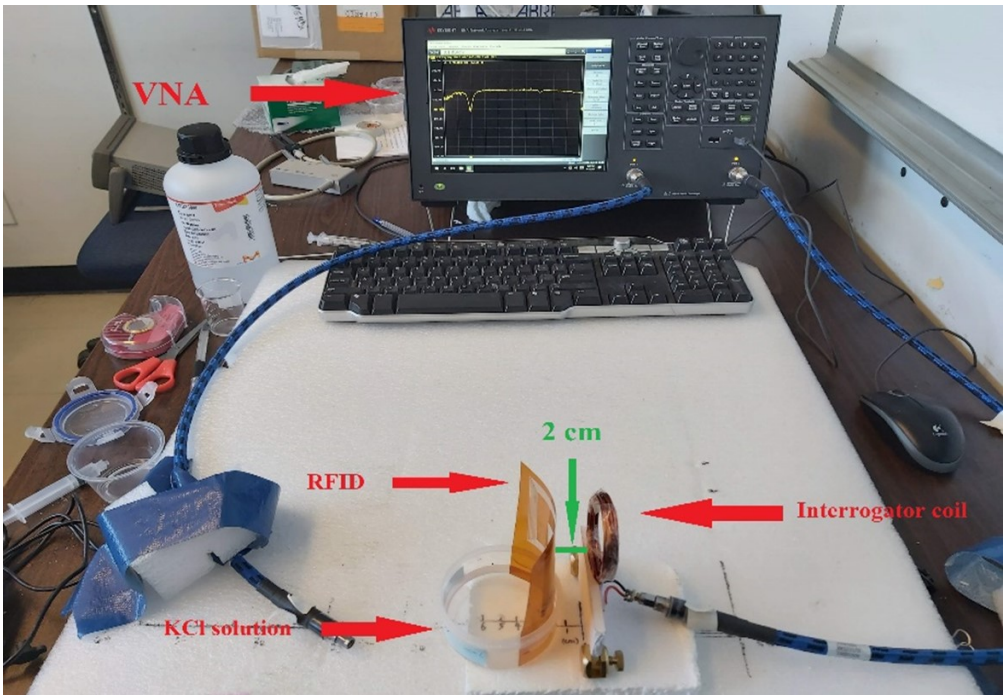

Figure 5.4 Experimental setup with coupled interrogator coil and RFID tag in a prepared KCl solution.

The experimental setup with coupled RFID tag sensor and interrogator coil for varying K^+ concentration is shown in Figure 5.4. The S11 of the interrogator coil is measured using a VNA (KEYSIGHT E5063A). Initially, the ISE is not in touch with any K^+ solution and the RIFD's resonant frequency is measured from the S11 response at the interrogator. Noted

that the interrogator coil is aligned concentrically with the printed inductor with a separation distance d = 2 mm to avoid over coupling issue. The resonant frequency of the RFID sensor is measured to be 19.97 MHZ, which matches well with the simulated and measured resonant frequency of the LC resonator printed on Kapton substrate obtained in chapter 4. The small frequency deviation is mainly due to the parasitic capacitance caused by jumping wires and conductive epoxy. Then, the ISE is connected to the prepared solutions of different K^+ molarity were poured up the container. The S11 at the interrogator coil (when coupled to the RFID sensor) for different KCL solutions is measured as shown in Figure 5.5. It is noticeable that the resonant frequency and quality factor would change for different K^+ molarity.

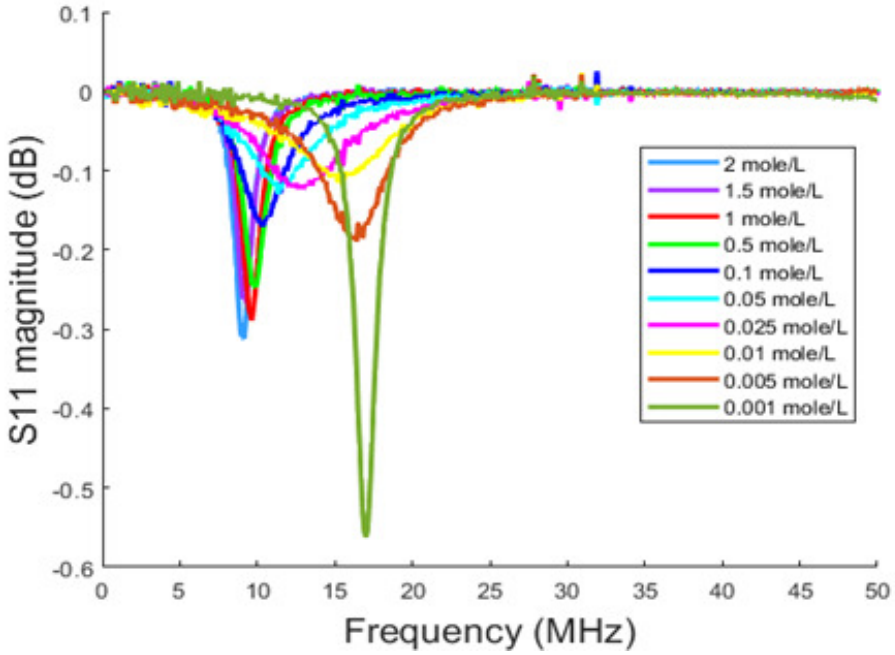

Figure 5.5 S11 measured at interrogator of RFID tag for different KCl concentrations.

For an ideal parallel RLC circuit, the resonant frequency occurs at $f_r = \frac{1}{2\pi\sqrt{LC}}$. The quality factor Q is defined as the ratio of the circulating branch current to the supply current.

For A parallel RLC circuit, its quality factor is in the form

$$Q = \frac{R}{X_L} = \frac{R}{\omega L} = \frac{R}{X_c} = R\omega C, Q^2 = R^2\frac{C}{L}, Q = R\sqrt{\frac{C}{L}}. \tag{5.4}$$

Therefore, the resonant frequency f_r of an ideal parallel RLC circuit is inversely proportional to the square root of the total capacitance in parallel. And, Q is proportional to the total resistance in parallel. In our case, as the K^+ selective electrodes connected with the LC resonator in parallel, the total capacitance C_{total} would be gradually dominated by C(K^+) as the K^+ molarity increases. f_r will drop sharply when K^+ molarity climbs at low molarity and maintains an almost steady value as K^+ molarity stays at a high level. In other words, the plot of resonant frequency f_r in terms of K^+ molarity should be the inverse of the electrode's capacitance measurement obtained in chapter 2. The plot of the quality factor Q concerning K^+ molarity should follow the same trend of the electrode's resistance measurement.

Figure 5.6 shows the resonant frequency of the RFID tag for different K^+ molarity solutions. Resonant frequencies were measured four times for each of 10 different KCL solutions to see the repeatability of the measurement. In between the measurements, the ISE was cleaned with DI water and dried with Kim wipes. As shown in Figure 5.6, an exponential fit is plotted given by

$$f_r\left(x\right) = 7.351 \times e^{-34.28x} + 10.01 \times e^{-0.038x} \tag{5.5}$$

where $f_r\left(x\right)$ and x represent f_r and K^+ molarity respectively. Over the 0.001-2mole/L K^+ dynamic range, Eqn. (5.5) represents the relationship between the resonant frequency and the K^+ molarity. Noted that the coefficient value -34.28 in the first exponential term is very closed to the negative inverse of the counterpart of ISE capacitance derived in chapter3 $\left(-\frac{1}{0.03} \approx -33.3\right)$. From the exponential fit, it was observed that the RFID sensor has an accuracy of 0.016 mole/L. The maximum difference among the measured data for the same

molarity was 0.89 MHz at 0.05 mole/L.

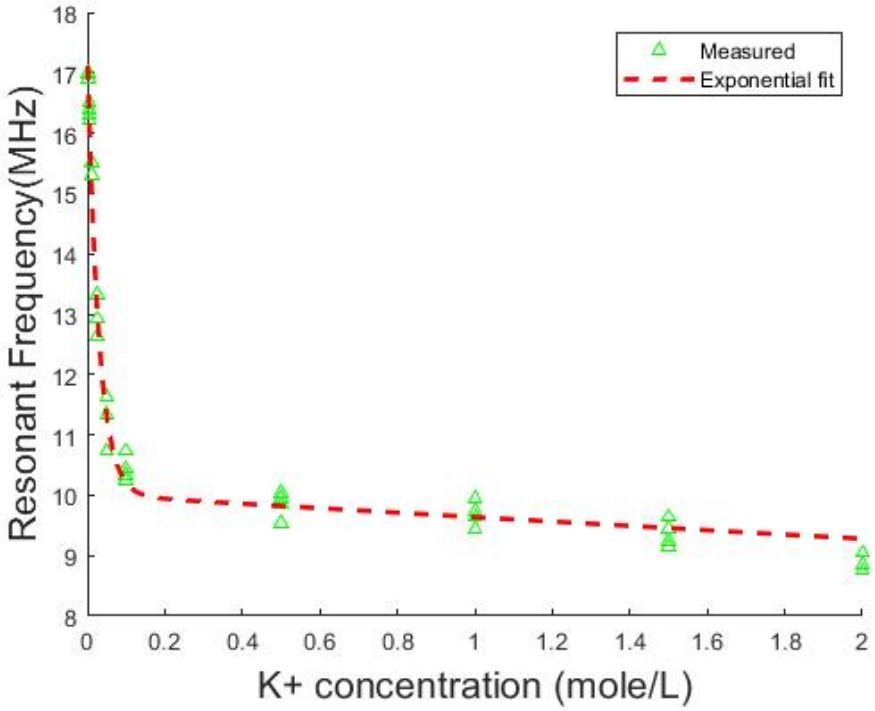

Figure 5.6 Resonant frequency of RFID tag for different KCl concentrations.

The measured quality factor in Figure 5.7 follows the trend of resistance variance shown in chapter3 as we assumed. However, the quality factor did not decrease monotonically as K^+ increases. We could hardly derive the correct K^+ concentration based on the quality factor especially when the Q value is between 3 and 7. So just like what we concluded in chapter2, quality factor based on the resistance across the ISE is not a suitable parameter for K^+ detection in practice. Therefore, only the resonant frequency of the RFID tag obtained from S11 of the interrogator coil can be used as a reliable tracking parameter for K^+ molarity detection.

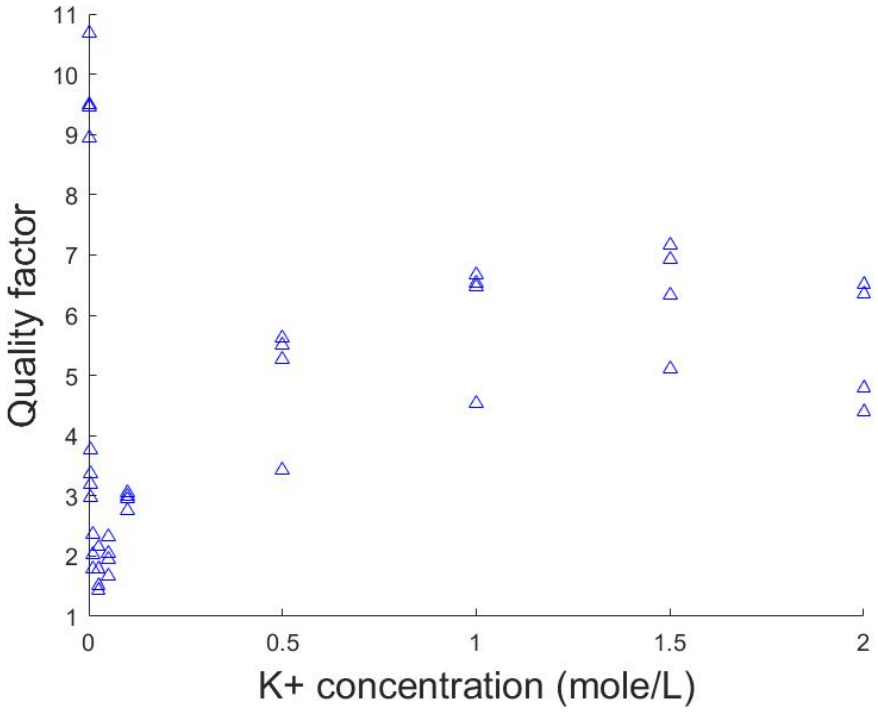

Figure 5.7 Quality factor of RFID tag for different KCl concentrations.

5.3 S11 and f_r Measurement for varying separation concentration

An experiment is conducted to measure the variation of the sensor's resonant frequencies with the separation distance for a test solution with constant K^+ concentration. Figure 5.8 displays the S11 measured at the interrogator for different separation distances. For all the trials, the K^+ ISE of the sensor is inserted into 1 mole/L KCl solution and the interrogator coil is aligned concentrically with the printed inductor. Here the separation distance is measured between the edge (the edge closer to the sensor) of the interrogator coil and the sensor. The magnitude of the S11 valley measured at the interrogator coil would decrease as the separation distance between the sensor and interrogator coil increases. From the valley of each S11 trial with a step size of 1 cm, it is evident that the magnitude of the magnetic field drops as $\frac{1}{R^6}$, where R is the distance between interrogator and tag.

According to the plot of each trial in Figure 5.8, a separation distance larger than 5

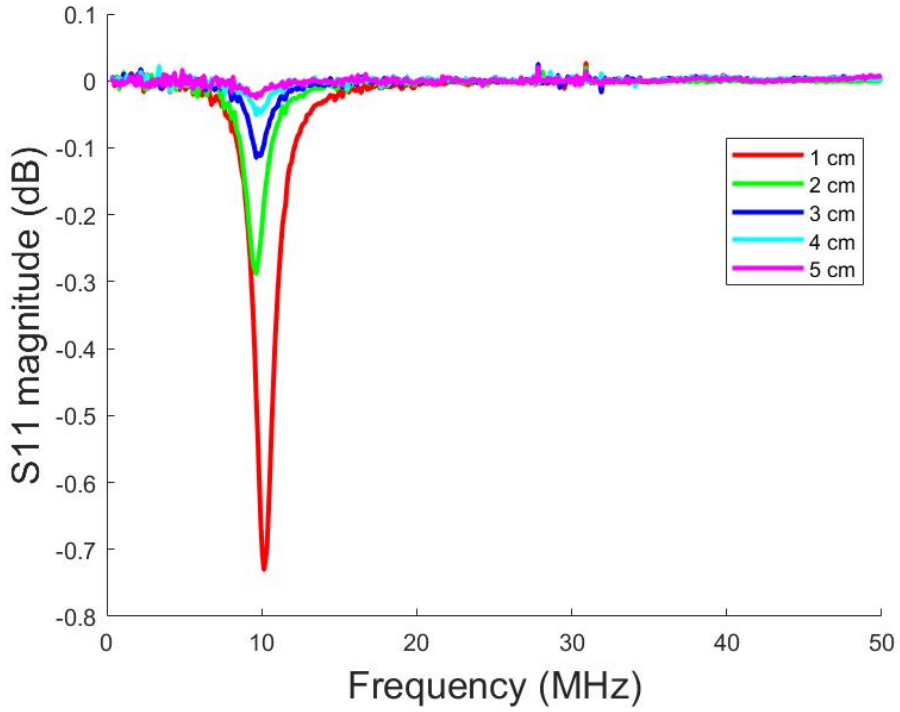

Figure 5.8 S11 measured at interrogator coil of RFID tag for different separation distance.

cm would lead to serious S11 signal attenuation that could not be measured. On the other hand, if the separation distance between the sensor and interrogator coil was too small, the resonant frequency shifts significantly due to the over-coupling effect. As illustrated in Figure 5.9, the resonant frequency is first at 10.14 MHz for 1 cm separation distance and then it will maintain a constant value of 9.64 MHz for 2 - 5 cm distance. It is important to keep a minimum separation distance of 2 cm between the integrator coil and RFID tag to obtain a steady resonant frequency. Therefore, a 2 - 5 cm operating distance should be ideal for the sensor. The maximum separation distance can be improved by increasing the power at the interrogator coil, or by increasing the number of turns and/or radius of the printed spiral inductor.

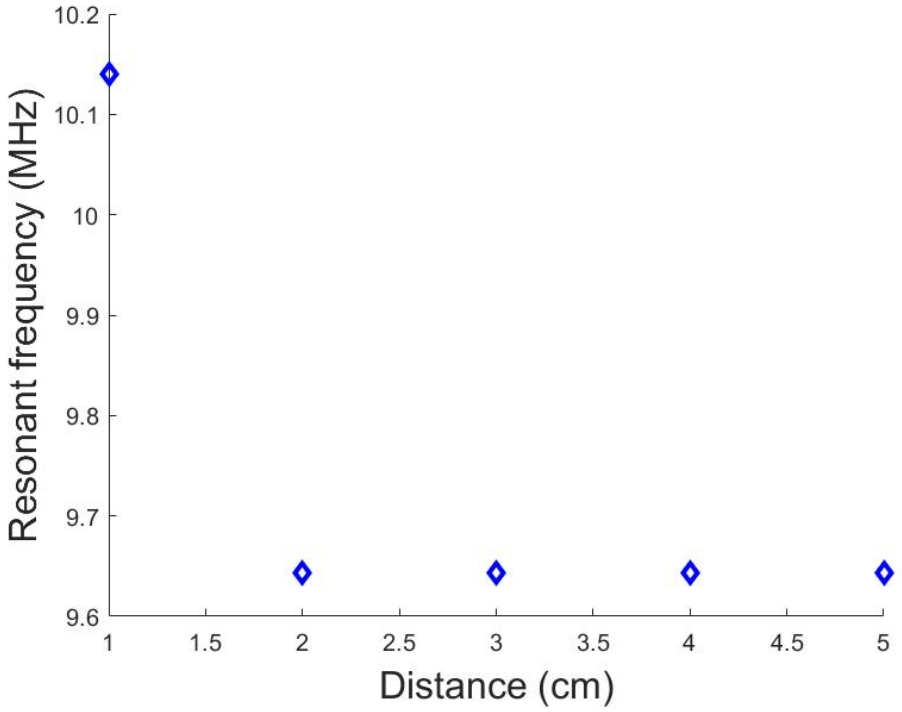

Figure 5.9 Resonant frequency of RFID tag with varying separation distance for 1 mole/L KCl.

5.4 Stability Test and Response Time

A stability experiment is conducted to measure the variation of resonant frequency with time. The sensor's ISE is inserted into a 1 mole/L KCl solution for seven days and the resonant frequency will be monitored every day. The separation distance between the sensor and the interrogator is set to be 2 cm and the printed inductor is aligned concentrically with the interrogator coil. The resonant frequency measured for the sensor on each day is plotted in Figure 5.10. The mean value of all the resonant frequencies in seven days is 9.6862 MHz and the standard deviation is 0.1609 MHz. The standard deviation was only 1.66% of the mean value. Such a low standard deviation indicated that all resonant frequencies were clustered close to the mean and the system was stable for one week. Thus, the prototype RFID tag is suitable for the long-term K^+ concentration tracking.

The response time of the RFID tag was remarkably short. As soon as the incorporated

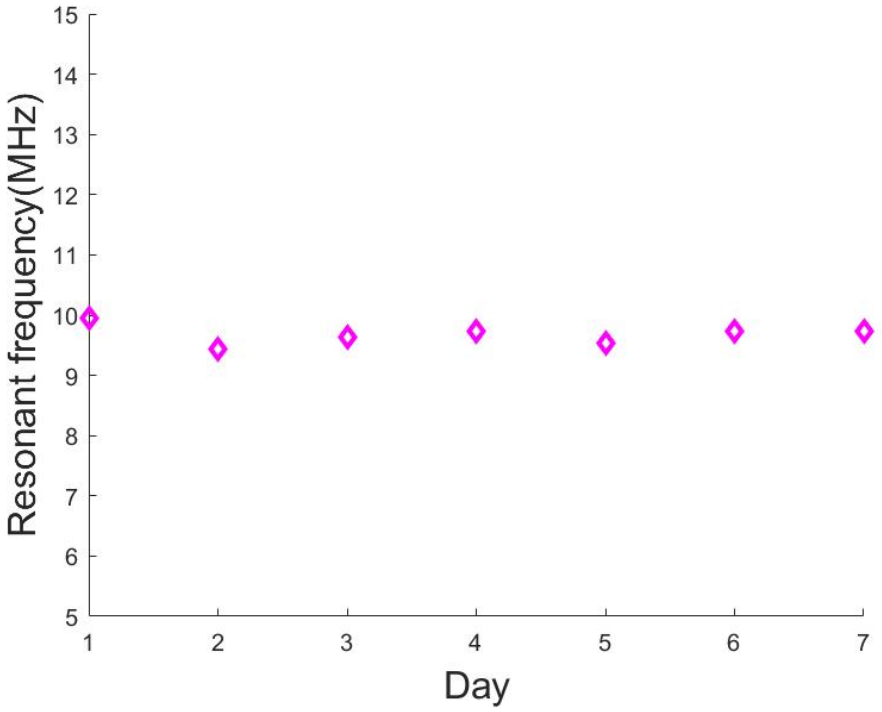

Figure 5.10 Resonant frequency of the RFID sensor measured over 7 days for 1 mole/L KCl solution.

ion-selective electrode of the RFID tag was inserted into the target solution, the S11 of the interrogator coil shifted to the corresponding valley immediately. The response time recorded for stable resonant frequency formation was smaller than 1 second concerning all KCl solutions used. In short, the prototype RFID tag could detect K^+ ions in solutions quickly within 1 second.

5.5 Temperature Test

All measurements shown above are performed at a constant room temperature of around 20°C. In practice, the resonant frequency of the RFID sensor is affected by temperature. As studied by Zahran et.al [65], thermodynamic parameters affect the selectivity for both ion exchangers and carrier ionophores of the K^+ ISE. Meanwhile, the ion selectivity change due to changing environmental temperature alters the ion fluxes between the membrane and the

solution. It will lead to the variance of both capacitance and resistance across the ISE, and the resonant frequency of the RFID sensor will shift accordingly. An experiment shown in Figure 5.11 is performed to investigate the variation of the sensor's resonant frequency with temperature. A Barnstead thermolyne is used to heat the KCl solution and the variation of the solution temperature is measured by the laser thermometer. The molarity of the KCl solution is set to be 1 mole/L constantly and the distance between the interrogator coil and RFID tag is 2 cm as before. The temperature of 1 mole/L KCl solution is increased from room temperature to 100°C and the resonant frequency of the RFID sensor is monitored.

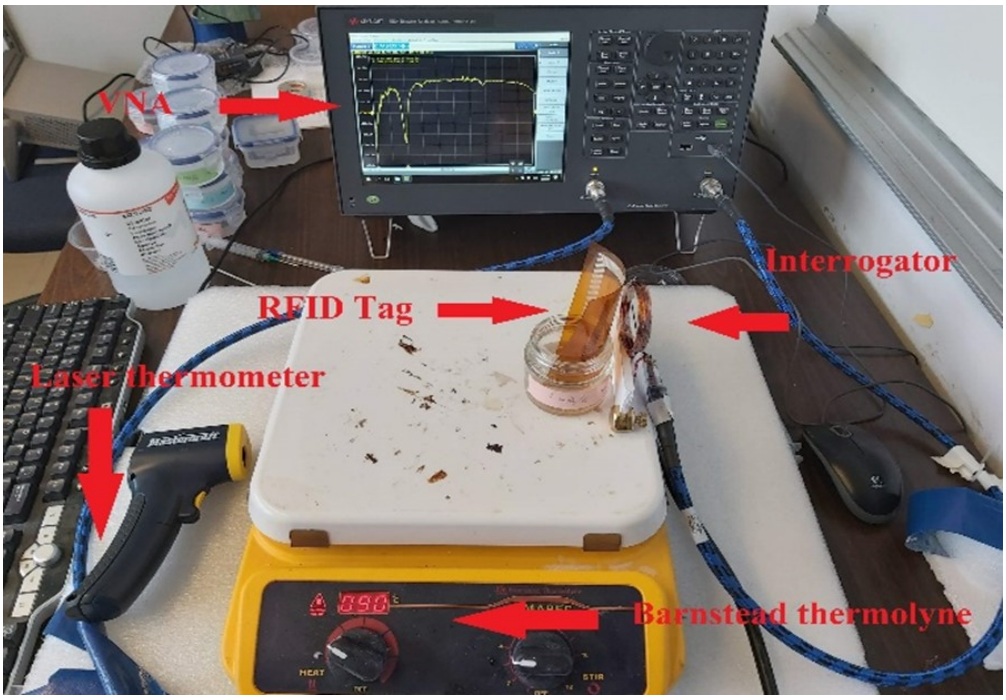

Figure 5.11 Experimental setup with coupled interrogator coil and RFID tag on a Barnstead thermolyne.

Figure 5.12 shows the S11 response of the coil interrogator obtained by VNA at different temperatures. The S11 valley would deviate more from the original response at room temperature as temperature increases.

Figure 5.13 demonstrates the resonant frequency of the RFID tag at different temperatures when the test KCl solution molarity is 1 mole/L. The 1st order linear fit for f_r is given

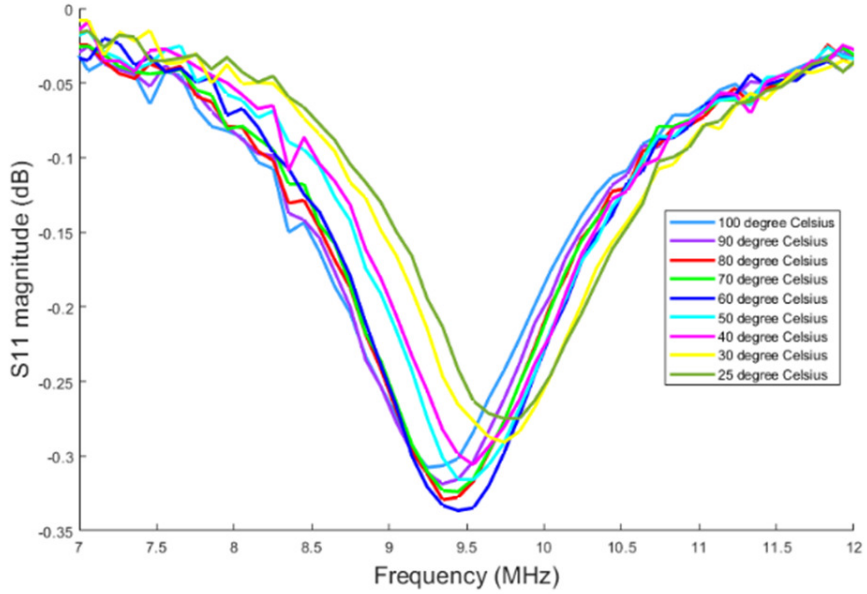

Figure 5.12 Measured S11 at interrogator of RFID tag for different temperatures.

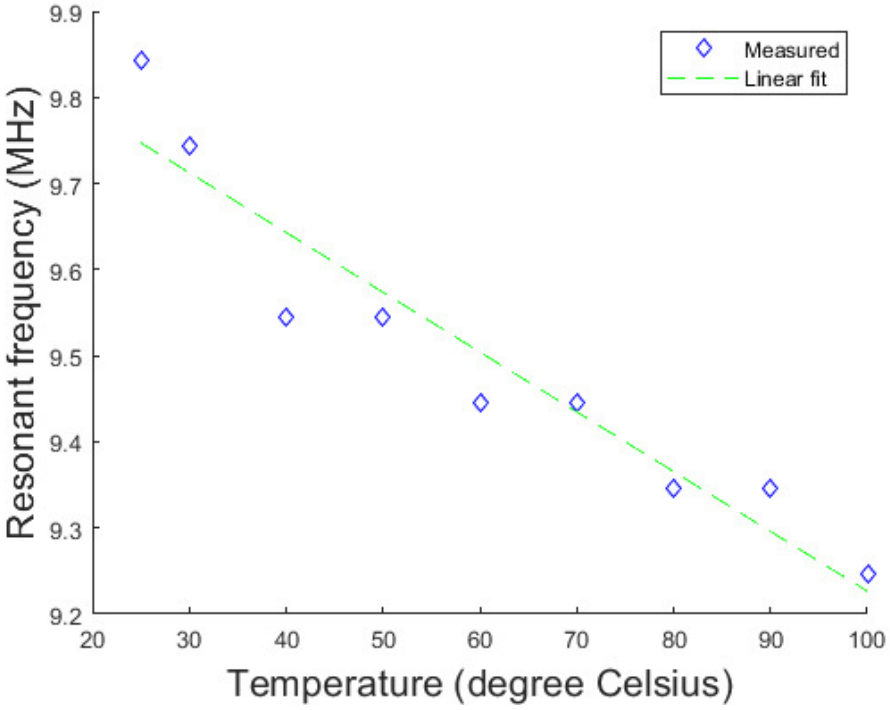

Figure 5.13 Resonant frequency of the RFID tag at different temperatures.

by

$$f_r(x) = -0.006944x + 9.921 \tag{5.6}$$

where $f_r(x)$ and x represent f_r and temperature respectively over the 25-100°C dynamic range. As the temperature increases, the ISE's capacitance rises. The resonant frequency decreases proportionally to the temperature increase. The minimum f_r is 9.246 Mhz at 100°C which is 0.6 MHz smaller than the counterpart at room temperature. This is an approximate 6% deviation and a temperature compensation technique for RFID layout may need to be implemented in the future.

In general, a flexible printed RFID sensor based on a printed LC resonator and ISE is fabricated for potassium ion sensing. The RFID sensor exhibited a second-order exponential relationship between the resonant frequency of the tag and the K^+ concentration of the solution over 0.001-2 mole/L dynamic range values. The RFID sensor achieved an accuracy of 0.016 mole/L. It has long-term stability in measurement. The response time of the RFID sensor is less than 1 second.

Chapter 6

Modified RFID Sensor Design

6.1 Design modification

To simplify the fabrication process and reduce the parasitic effect caused by the jumper wires, the proposed RFID sensor layout can be modified to a double-layer configuration. Instead of using jumping wires, we could print the conductive wires on the rear side of the Kapton substrate to connect the spiral inductor and interdigital capacitor in parallel. A couple of copper rivets were added to connect both sides of the design on the substrate through via holes. Figure 6.1 illustrates both sides of the modified RFID sensor.

6.2 S11 and f_r Measurement for varying K^+ concentration

The same experimental setup shown in Figure 5.6 was used to measure the wireless performance of the modified RFID sensor. The interrogator coil was aligned concentrically with the printed inductor with a separation distance d = 2 cm. KCl solutions with varying K^+ concentrations between 0.001 mole/L to 2 mole/L were fabricated for testing at room temperature. Figure 6.2 shows a sample of the measured S11 at the interrogator coil for

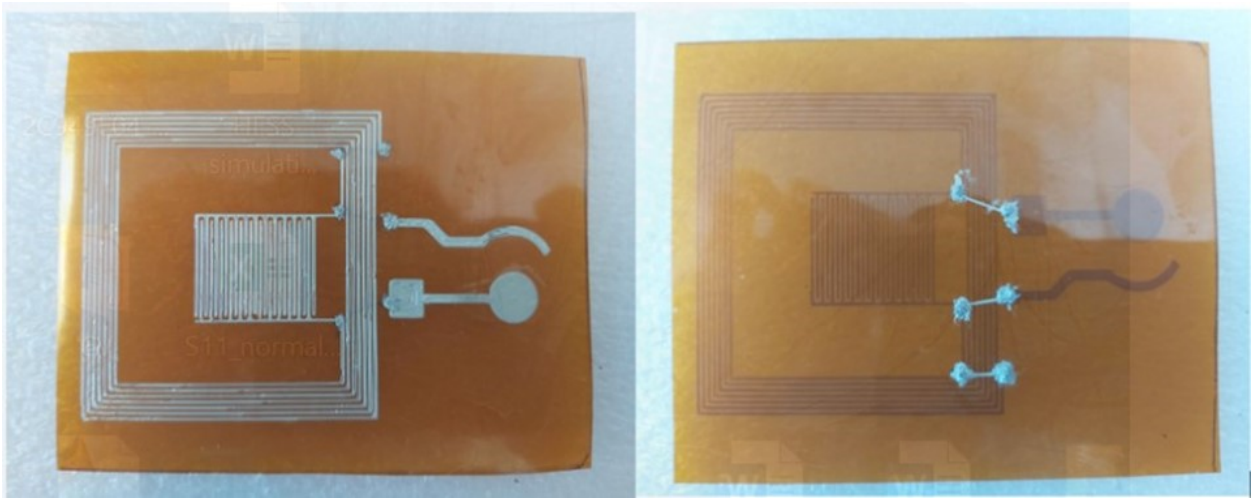

Figure 6.1 modified RFID tag printed for K+ sensing (left for front layout and right for rear layout).

different K^+ solutions.

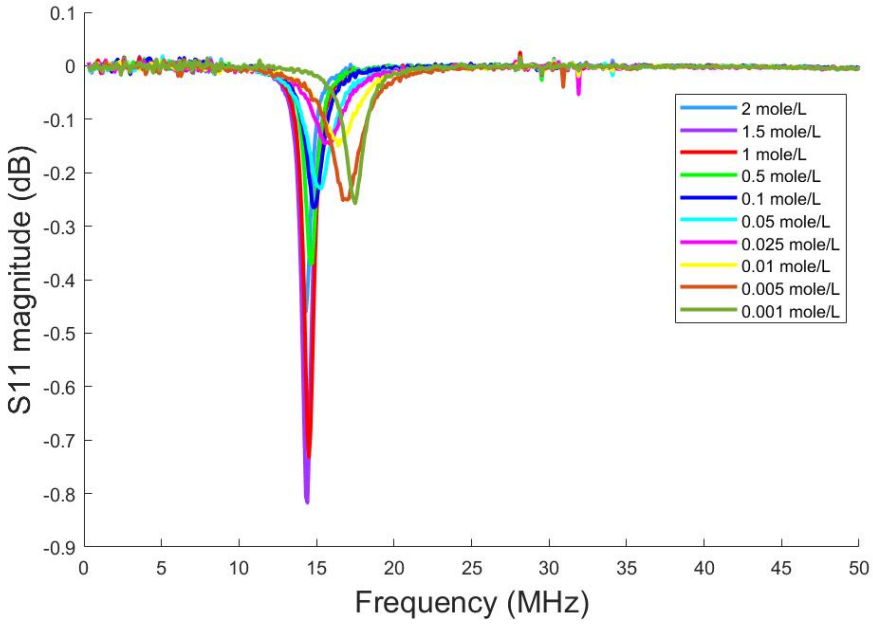

Figure 6.2 S11 measured at interrogator of modified RFID tag for different KCl concentrations.

Figure 6.3 plots the resonant frequency of the RFID tag for different K^+ molarity solutions based on S11 measurement. Resonant frequencies were measured four times for each of 10 different KCl solutions to see the repeatability of the measurement. As shown in Figure 6.3,

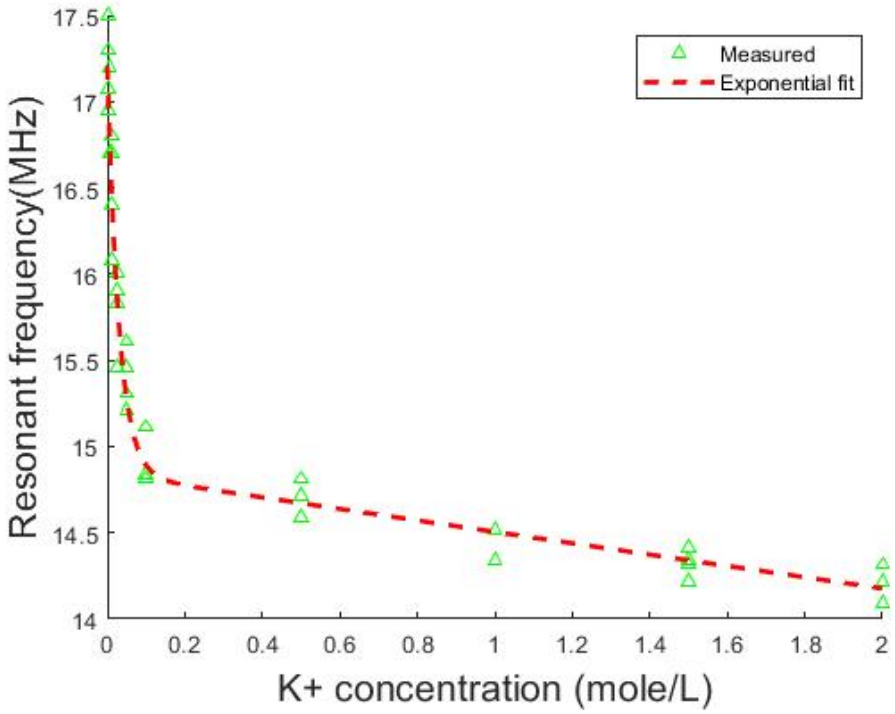

Figure 6.3 Resonant frequency of modified RFID for different K^+ concentrations.

an exponential fit was given by

$$f(x) = 2.737 \times e^{-33.180x} + 14.840 \times e^{-0.023x} \tag{6.1}$$

where $f_r(x)$ and x represent f_r and K^+ molarity respectively, fits to the measured data. Eqn. (5.7) exhibits an 2^{nd} order exponential relationship between the resonant frequency and the K^+ molarity over the 0.001-2 mole/L K+dynamic range. Noted that the coefficient value -33.180 in the first exponential term is also closed to the negative inverse of the counterpart in Eqn. (3.1) ($\frac{-1}{0.03} \approx -33.3$). It is a convincible parameter since the capacitor controlled by the ISE is inversely proportional to the sensor's resonant frequency. Also, the resonant frequency for each K+ molarity is higher than the counterpart of the unmodified RFID, which indicated that the parasitic capacitance brought by the via and copper rivets is smaller. From the exponential fit, it was observed that the RFID sensor has an accuracy of 0.0136 mole/L

for low K^+ concentration solutions. The maximum difference among the measured data for the same molarity was 0.547 MHz at 0.001 mole/L.

6.3 S11 and f_r Measurement for varying separation distance

Based on previous experience, it was critical to keep a minimum separation distance between the interrogator coil and the RFID sensor to avoid over coupling effect. Meanwhile, as the separation distance between the sensor coil and the interrogator coil increases, the received signal amplitude from the sensor attenuates. An experiment was conducted to measure the variation of the sensor's resonant frequency with the separation distance 1mole/L KCl. Figure 6.4 demonstrates the S11 recorded at the interrogator for 1 mole/L KCL solution with varying distance.

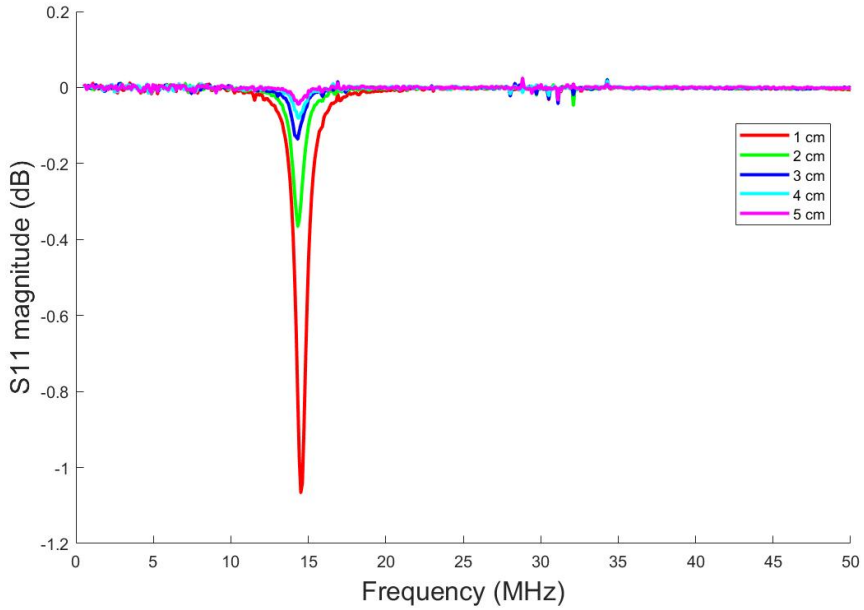

Figure 6.4 S11 with varying separation distance between the interrogator and modified sensor for 1 mole/L KCl.

Figure 6.5 illustrates the resonant frequency received from the sensor for different separation distance conditions. According to Figure 6.5, distances less than 2 cm set the sensor

in the over coupling region and a maximum separation distance of 5 cm was founded to maintain a readable resonance amplitude (the largest acceptable S11 signal attenuation). It is essential to keep a minimum separation distance of 2 cm between the integrator coil and RFID tag to obtain a steady resonant frequency. Therefore, a 2-5 cm operating distance should be ideal for the modified RFID sensor.

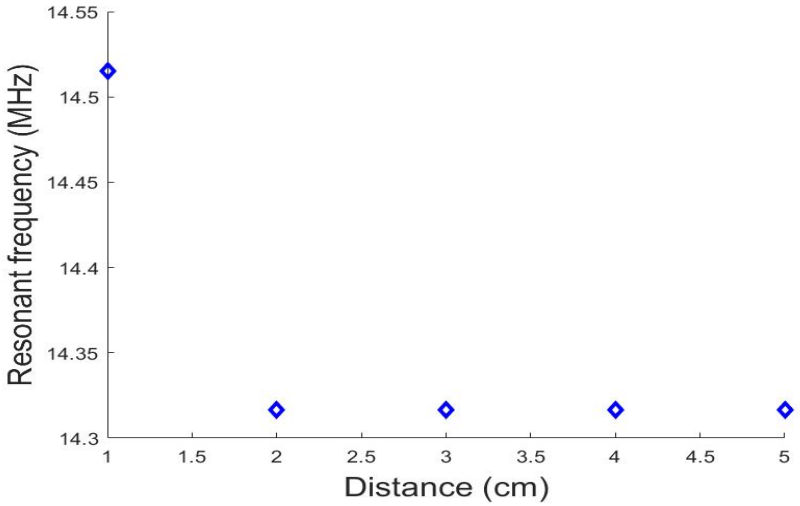

Figure 6.5 Resonant frequency of modified RFID sensor with different separation distance for 1 mole/L KCL

6.4 Stability Test and Response Time

A long-term stability experiment was conducted to measure the variation of resonant frequency with time. It recorded the f_r data of the RFID that was inserted into 1 mole/L KCl solution for seven days. The separation distance between the sensor and the interrogator was set to be 2 cm and the printed inductor was aligned concentrically with the interrogator coil. The resonant frequency measured for the sensor on each day is plotted in Figure 6.6. The mean value of all the resonant frequencies in seven days is 14.3869 MHz and the standard deviation is 0.0677 MHz. The standard deviation was only 0.4635% of the mean value. Its is a lower standard deviation than the counterpart derived for the RFID tag

without modification. It indicated that all resonant frequencies were clustered close to the mean and the system was stable for one week. Thus, the modified RFID tag is more suitable for the long-term K^+ concentration tracking.

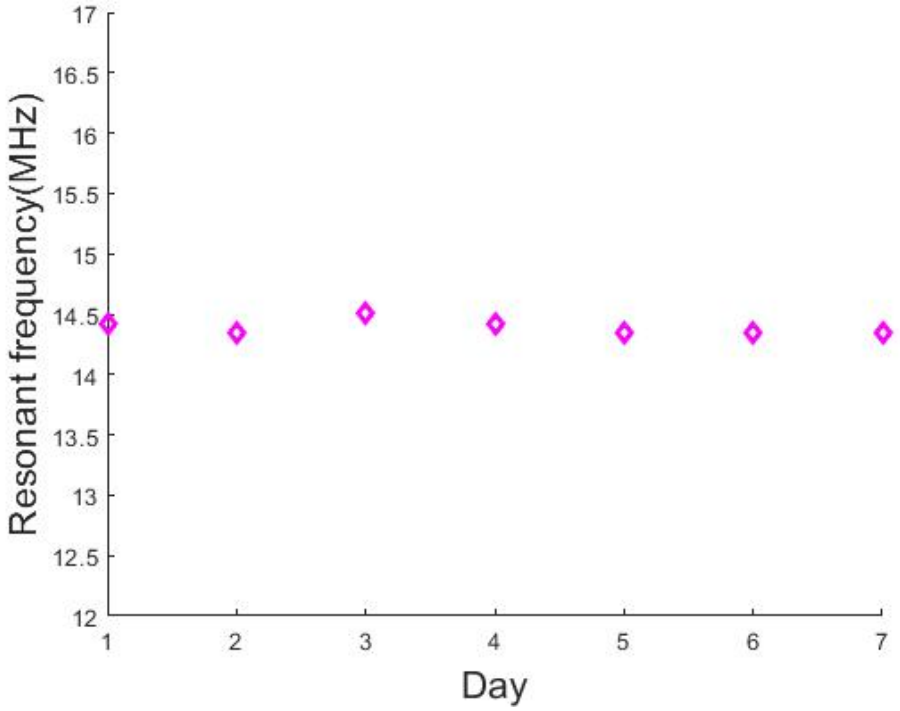

Figure 6.6 Resonant frequency of the modified sensor measured over 7 days for 1 mole/L KCl solution.

The response time of the RFID tag was still small. Noted that the time recorded for stable resonant frequency formation was always smaller than 1 second concerning all KCl solutions used. In short, the modified RFID tag could detect K^+ ions in solutions quickly within 1 second.

6.5 Temperature Test

An experiment shown in Figure 5.11 was performed to investigate the variation of the sensor's resonant frequency with temperature. A Barnstead thermolyne was used to heat the KCl solution and the variation of the solution temperature is measured by the laser

thermometer. The molarity of the KCl solution was set to be 1 mole/L constantly and the distance between the interrogator coil and RFID tag was 2 cm as before. The temperature of 1 mole/L KCl solution was increased from room temperature to 100°C and the resonant frequency of the RFID sensor is monitored. Figure 6.7 shows the S11 response of the coil interrogator obtained by VNA at different temperatures. The S11 valley would deviate more from the original response at room temperature as temperature increases due to more active ion fluxes between the membrane and the solution.

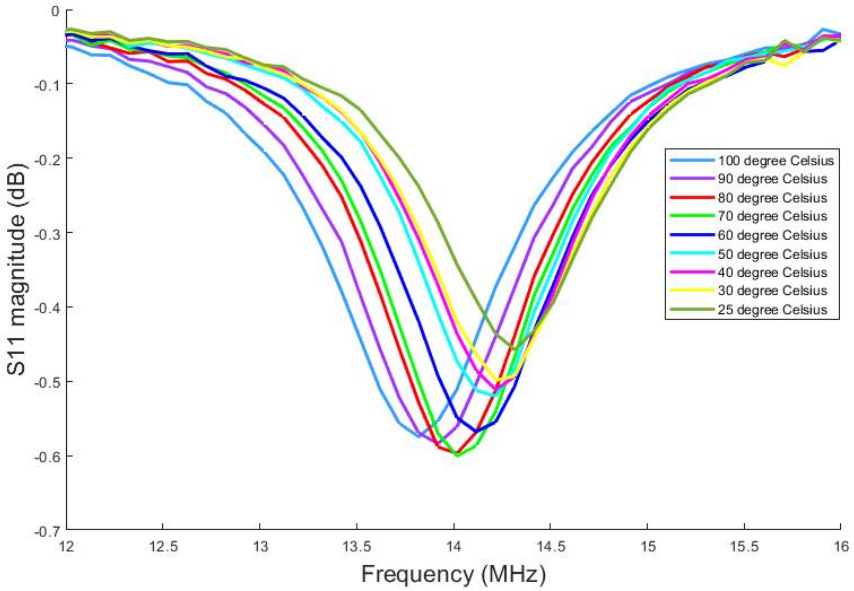

Figure 6.7 Measures S11 of modified RFID sensor at different temperature for 1 mole/L KCl solution.

Figure 6.8 shows the resonant frequency of the RFID tag at different temperature when the test KCl solution molarity is 1 mole/L. The 1^st order linear fit for f_r is given by

$$f_r(x) = -0.005992x + 14.46 \tag{6.2}$$

where $f_r(x)$ and x represent f_r and temperature respectively over the 25-100°C dynamic range. As the temperature increases, the ISE's capacitance rises. The resonant frequency

decreases proportionally to the temperature increase. The minimum f_r is 13.8196 MHz at 100°C which is 0.497 MHz smaller than the counterpart at room temperature. This is an approximate 3.47% deviation, and it is smaller than the previous deviation value obtained for unmodified RFID sensor. Thus, the temperature stability of the modified sensor is better.

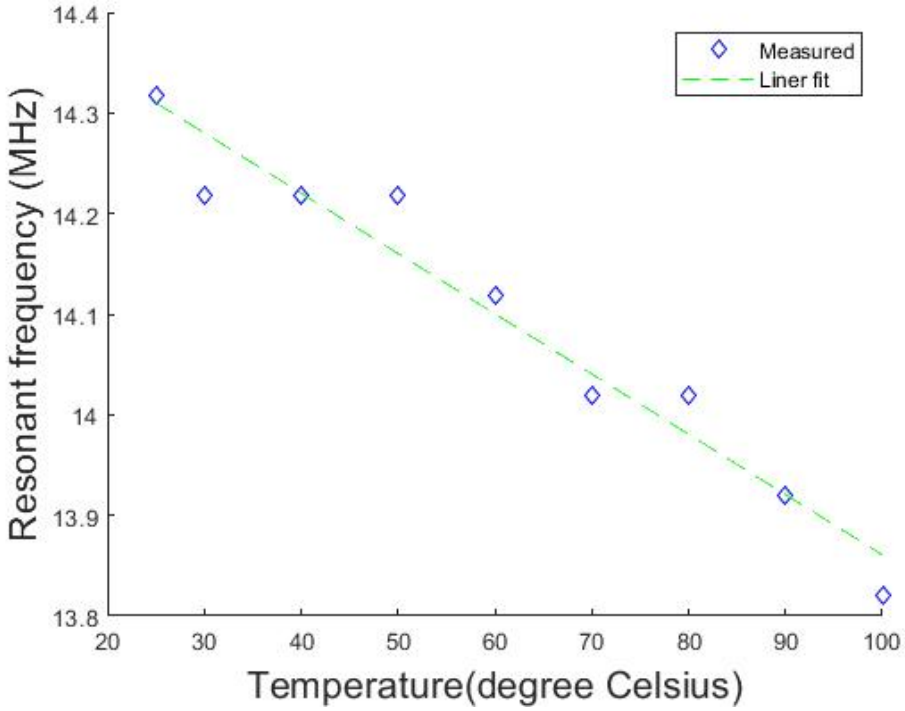

Figure 6.8 Resonant frequency of the modified RFID sensor at different temperatures for 1 mole/L KCl solution.

To sum up, the modified double-layer RFID sensor has higher operating resonant frequency as the parasitic capacitance was reduced after modification. The reading distance of the modified RFID sensor is still 2-5 cm since the printed inductor is unchanged. However, based on measurement, the long term stability and temperature stability of the modified RFID sensor are better than that of the original RFID sensor. The usage of via holes and copper rivets improves the wireless performance of the RFID sensor.

Chapter 7

Conclusion and Future Work

7.1 Conclusion

This thesis studies and develops the design of a flexible printed chipless RFID sensor for remote potassium (K^+) ion sensing. The proposed RFID sensor is composed of an inductive-capacitive (LC) resonator and a K^+ ion-sensitive electrode (ISE). Initially, the LC resonator consisting of a planar spiral inductor and an interdigital capacitor is designed and fabricated by the inkjet-printing technology on a flexible Kapton film substrate. Then, an ISE for potassium ion sensing is printed on the Kapton film, followed by casting prepared ion sensitive membrane on the sensing electrode. The potassium ion concentration of the contact solution can be wirelessly monitored by measuring the change of the RFID sensor's resonant frequency. The RFID sensor exhibits a second-order exponential relationship between the resonant frequency of the sensor and the K^+ concentration of the solution over the measurement range. It achieves an accuracy of 0.016 mole/L and has a response time of less than 1 second. The temperature and long-term stability experiments demonstrate its potential for measuring K^+ of solution in a long period. In the next part of the thesis, the design of the original RFID sensor is modified to improve its wireless performance by using via holes and copper rivets. The resulted double-layer RFID sensor achieves an accuracy of 0.0136

mole/L. It also has better long-term stability and temperature stability than that of the original RFID sensor. The fabrication process of the proposed RFID sensor is simple and fast due to the usage of printing technology. The flexibility of the Kapton film substrate makes the sensor conformal to different types of surfaces. Meanwhile, it is a passive sensor that requires no external power supply, making it suitable for long-term monitoring without charging or replacing batteries. As a result, the prototype RFID sensor performs well and has great potential for low-cost K^+ monitoring applications.

7.2 Future Work

In the future, more types of ion membranes can be coated on the ISE of the proposed sensor to measure different ions in contact solution. The cross sensitivity of the RFID sensor can be further explored and studied for better prospects. The limitation of the interrogation distance can be improved for the modification of the printed inductor in the future. A multiple-layer stacked inductor presented by Ashraf [66] can be employed to increase the inductance and reading range. Since the performance of the RFID tag is affected by the environmental temperature. Future research can investigate the temperature compensation technique applied to sensor electronics to reduce the deviation of the RFID sensor's resonant frequency.

Bibliography

[1] Moncef Tounsi, Mourad Ben Braiek, Abdellatif Baraket, Michael Lee, Nadia Zine, M. Zabala, Joan Bausells, Faouzi Aloui, Béchir Hassine, Abderrazak Maaref, and A. Errachid. Electrochemical capacitive k + emis chemical sensor based on the dibromoaza[7]helicene as an ionophore for potassium ions detection. *Electroanalysis*, 28, 06 2016.

[2] D. C. Gadsby, R. Niedergerke, and S. Page. Do intracellular concentrations of potassium or sodium regulate the strength of the heart beat? *Nature*, 232(5313):651 – 653, 1971.

[3] A. J. Hansen, J. Hounsgaard, and H. Jahnsen. Anoxia increases potassium conductance in hippocampal nerve cells. *Acta Physiologica Scandinavica*, 115(3):301–310, 1982.

[4] Ria Arnold, Timothy Pianta, Bruce Pussell, Zoltan Endre, Matthew Kiernan, and Arun Krishnan. Potassium control in chronic kidney disease: Implications for neuromuscular function. *Internal Medicine Journal*, 49, 09 2018.

[5] W. F. Ganong. *Review of medical physiology*. McGraw-Hill Medical, New York, 2005.

[6] Astrid Sigel, Helmut Sigel, and Roland Sigel. *Interrelations between Essential Metal Ions and Human Diseases*. 01 2013.

[7] Zafar Israili, Rafael Hernández Hernández, and Manuel Velasco. The future of antihypertensive treatment. *American journal of therapeutics*, 14:121–34, 03 2007.

[8] Ihab Hajjar and Theodore Kotchen. Trends in prevalence, awareness, treatment, and control of hypertension in the united states, 1988-2000. *JAMA : the journal of the American Medical Association*, 290:199–206, 08 2003.

[9] Laura Svetkey, Denise Simons-Morton, Michael Proschan, Frank Sacks, Paul Conlin, Davis Harsha, and Thomas Moore. Effect of the dietary approaches to stop hyper-

tension diet and reduced sodium intake on blood pressure control. *Journal of clinical hypertension (Greenwich, Conn.)*, 6:373–81, 07 2004.

[10] William Cushman and Jan Basile. Achieving blood pressure goals: Why aren't we? *Journal of clinical hypertension (Greenwich, Conn.)*, 8:865–72, 01 2007.

[11] Ihab Hajjar, Jane Kotchen, and Theodore Kotchen. Hajjar i, kotchen jm, kotchen ta. hypertension: trends in prevalence, incidence, and control. *Annual review of public health*, 27:465–90, 02 2006.

[12] Mark Houston. The importance of potassium in managing hypertension. *Current hypertension reports*, 13:309–17, 03 2011.

[13] Christopher Sobey. Potassium channel function in vascular disease. *Arteriosclerosis, thrombosis, and vascular biology*, 21:28–38, 02 2001.

[14] Undurti N. Das. Nutritional factors in the pathobiology of human essential hypertension. *Nutrition*, 17(4):337–346, 2001.

[15] Yousri M. Barri and Charles S. Wingo. The effects of potassium depletion and supplementation on blood pressure: A clinical review. *The American Journal of the Medical Sciences*, 314(1):37–40, 1997.

[16] Weizhong Ying, Kristal Aaron, Pei-Xuan Wang, and Paul Sanders. Potassium inhibits dietary salt-induced transforming growth factor-beta production. *Hypertension*, 54:1159–63, 10 2009.

[17] Makiko Kido, Katsuyuki Ando, Maristela Onozato, Akihiro Tojo, Masahiro Yoshikawa, Teruhiko Ogita, and Toshiro Fujita. Protective effect of dietary potassium against vascular injury in salt-sensitive hypertension. *Hypertension*, 51:225–31, 03 2008.

[18] Linda Mierlo, Arno Greyling, Peter Zock, F.J. Kok, and Johanna Geleijnse. Suboptimal potassium intake and potential impact on population blood pressure. *Archives of internal medicine*, 170:1501–2, 09 2010.

[19] B. Fennani, Habib Hamam, and Adel Dahmane. Rfid overview. pages 1–5, 12 2011.

[20] H. Stockman. Communication by means of reflected power. *Proceedings of the IRE*, 36:1196 – 1204, 11 1948.

[21] Liu Chunli. Application and development of rfid technique. 04 2012.

[22] Michael Maloni. Understanding radio frequency identification (rfid) and its impact on the supply chain. 01 2006.

[23] Vipul Chawla and Dong Ha. An overview of passive rfid. *Communications Magazine, IEEE*, 45:11 – 17, 10 2007.

[24] Pavel Nikitin and K.V.s Rao. Performance limitations of passive uhf rfid systems. pages 1011–1014, 01 2006.

[25] Daniel Deavours. Improving the near-metal performance of uhf rfid tags. pages 187 – 194, 05 2010.

[26] Cornel Turcu. *Current Trends and Challenges in RFID*. IntechOpen, London, July 2011.

[27] Tengku Norliza, Tengku Norliza Tengku Mohamad, Jahariah Sampe, Md Islam, and Dilla Berhanuddin. Architecture of micro energy harvesting using hybrid input of rf, thermal and vibration for semi- active rfid tag. *Engineering Journal*, 21:183–197, 03 2017.

[28] Konstantin N. Mikhelson. *Ion-Selective Electrodes*. Springer, New York, 2013.

[29] Eric Bakker, Philippe Bühlmann, and Ernö Pretsch. Carrier-based ion-selective electrodes and bulk optodes. 1. general characteristics. *Chemical Reviews*, 97(8):3083–3132, 1997. PMID: 11851486.

[30] G. Orellana, C. Cano-Raya, J. López-Gejo, and A.R. Santos. 3.10 - online monitoring sensors. In Peter Wilderer, editor, *Treatise on Water Science*, pages 221–261. Elsevier, Oxford, 2011.

[31] N. Stradiotto, H. Yamanaka, and M. Zanoni. Electrochemical sensors: a powerful tool in analytical chemistry. *Journal of the Brazilian Chemical Society*, 14:159–173, 2003.

[32] A. Bratov, N. Abramova, and A. Ipatov. Recent trends in potentiometric sensor arrays—a review. *Analytica Chimica Acta*, 678(2):149–159, 2010.

[33] Joaquín A. Ortuño, Francisca Tomás-Alonso, and Aurora M. Rubio. Chapter 9 - ion-selective electrodes based on ionic liquids. In Antonia Pérez De Los Ríos and Francisco José Hernández Fernández, editors, *Ionic Liquids in Separation Technology*, pages 275–299. Elsevier, Amsterdam, 2014.

[34] M. Sohail and R. De Marco. Electrodes — ion-selective electrodes. In *Reference Module in Chemistry, Molecular Sciences and Chemical Engineering*. Elsevier, 2013.

[35] Dorota Pijanowska and Wladyslaw Torbicz. Ion selective and semi-permeable membranes for biosensors in biomedical applications. *Biocybernetics and Biomedical Engineering*, 28:11–19, 01 2008.

[36] Arokia Nathan, Arman Ahnood, Matthew Cole, Yuji Suzuki, Pritesh Hiralal, Francesco Bonaccorso, Tawfique Hasan, Luis Garcia-Gancedo, R. Chen, Piers Andrew, S. Hoffman, Daping Chu, Andrew Flewitt, Andrea Ferrari, M.J. Kelly, J. Robertson, Gehan Amaratunga, and W. Milne. Flexible electronics: The next ubiquitous platform. *Proceedings of the IEEE*, 100:1486, 05 2012.

[37] Wen-Yang Chang, Te-Hua Fang, Heng-Ju Lin, Yu-Tang Shen, and Yu-Cheng Lin. A large area flexible array sensors using screen printing technology. *IEEE/OSA Journal of Display Technology - J DISP TECHNOL*, 5:178–183, 06 2009.

[38] Minhun Jung, Jaeyoung Kim, Jinsoo Noh, Namsoo Lim, Chaemin Lim, Gwangyong Lee, Junseok Kim, Hwiwon Kang, Kyunghwan Jung, Ashley Leonard, James Tour, and Gyoujin Cho. All-printed and roll-to-roll-printable 13.56-mhz-operated 1-bit rf tag on plastic foils. *Electron Devices, IEEE Transactions on*, 57:571 – 580, 04 2010.

[39] Andreas Sandström, Henrik Dam, Frederik Krebs, and Ludvig Edman. Ambient fabrication of flexible and large-area organic light-emitting devices using slot-die coating. *Nature communications*, 3:1002, 08 2012.

[40] Brian Derby. Additive manufacture of ceramics components by inkjet printing. *Engineering*, 1, 03 2015.

[41] Madhusudan Singh, Hanna Haverinen, Parul Dhagat, and Ghassan Jabbour. Inkjet printing-process and its applications. *Advanced materials (Deerfield Beach, Fla.)*, 22:673–85, 02 2010.

[42] Heba Mohamed. Screen-printed disposable electrodes: Pharmaceutical applications and recent developments. *TrAC Trends in Analytical Chemistry*, 82, 02 2016.

[43] Rozalia Szentgyörgyvölgyi. 12 - gravure printing. In Joanna Izdebska and Sabu Thomas, editors, *Printing on Polymers*, pages 199–215. William Andrew Publishing, 2016.

[44] Saleem Khan, Ravinder Dahiya, and Leandro Lorenzelli. Technologies for printing sensors and electronics over large flexible substrates: A review. *IEEE Sensors Journal*, PP, 12 2014.

[45] Bogdan Adamczyk. *Foundations of Electromagnetic Compatibility: with Practical Applications*. John Wiley & Sons Ltd., New York, February 2017.

[46] Hubert Aebischer. Inductance formula for square planar spiral inductors with rectangular conductor cross section. *Advanced Electromagnetics*, 9, 09 2019.

[47] E. Pettenpaul, H. Kapusta, A. Weisgerber, H. Mampe, Jürgen Luginsland, and Ingo Wolff. Cad models of lumped elements on gaas up to 18 ghz. *Microwave Theory and Techniques, IEEE Transactions on*, MTT-36:294 – 304, 03 1988.

[48] Franz Ollendorff. *Berechnung magnetischer Felder*. Springer, Vienna, 1952.

[49] FREDERICK EMMONS TERMAN. *RADIO ENGINEERS' HANDBOOK*. McGRAW -HILL BOOK COMPANY, INC., NEW YORK AND LONDON, 1943.

[50] S.S. Mohan, M. del Mar Hershenson, S.P. Boyd, and T.H. Lee. Simple accurate expressions for planar spiral inductances. *IEEE Journal of Solid-State Circuits*, 34(10):1419–1424, 1999.

[51] H.A. Wheeler. Simple inductance formulas for radio coils. *Proceedings of the Institute of Radio Engineers*, 16(10):1398–1400, 1928.

[52] Ashraf Islam. Design and optimization of printed circuit board inductors for wireless power transfer system. *Circuits and Systems*, 04:237–244, 01 2013.

[53] Almudena Rivadeneyra, José F. Salmerón, Manuel Agudo, J.A. López-Villanueva, Luis Fermin Capitan-Vallvey, and Alberto Palma. Design and characterization of a low thermal drift capacitive humidity sensor by inkjet-printing. *Sensors and Actuators B: Chemical*, 195:123–131, 05 2014.

[54] Kenichi Morimoto, Yutao Qin, and Yogesh Gianchandani. Modeling and characterization of the transient performance of a gas detector based on fringe-field capacitance. *Proceedings of IEEE Sensors*, 2014:1843–1846, 12 2014.

[55] F. Molina-Lopez, Thomas Kinkeldei, D. Briand, G. Troster, and N.F. Rooij. Theoretical and experimental study of the bending influence on the capacitance of interdigitated micro-electrodes patterned on flexible substrates. *Journal of Applied Physics*, 114:174907–174907, 11 2013.

[56] Gray Alley. Interdigital capacitors and their application to lumped-element microwave integrated circuits. *Microwave Theory and Techniques, IEEE Transactions on*, 18:1028 – 1033, 01 1971.

[57] David Lacombe and Jerome Cohen. Octave-band microstrip dc blocks (short papers). *Microwave Theory and Techniques, IEEE Transactions on*, 20:555 – 556, 09 1972.

[58] John Hobdell. Optimization of interdigital capacitors. *Microwave Theory and Techniques, IEEE Transactions on*, 27:788– 791, 10 1979.

[59] K. Neupert-Laves and M. Dobler. The crystal structure of a k+ complex of valinomycin. *Helvetica chimica acta*, 58 2:432–42, 1975.

[60] Mohsen Zareh. *Plasticizers and Their Role in Membrane Selective Electrodes*. 03 2012.

[61] ZhangFei Su, XueQin Ran, J. Jay Leitch, Adrian L. Schwan, Robert Faragher, and Jacek Lipkowski. How valinomycin ionophores enter and transport k+ across model lipid bilayer membranes. *Langmuir*, 35(51):16935–16943, 2019. PMID: 31742409.

[62] George. Horvai, Etelka. Graf, Klara. Toth, Erno. Pungor, and Richard P. Buck. Plasticized poly(vinyl chloride) properties and characteristics of valinomycin electrodes. 1.

high-frequency resistances and dielectric properties. *Analytical Chemistry*, 58(13):2735–2740, 1986.

[63] Jan Rainey, Jeffrey DeVries, and Brian Sykes. Estimation and measurement of flat or solenoidal coil inductance for radiofrequency nmr coil design. *Journal of magnetic resonance (San Diego, Calif. : 1997)*, 187:27–37, 08 2007.

[64] F Grover. *Inductance Calculations*. 01 1964.

[65] Elsayed Zahran, Vasileios Gavalas, Manuel Valiente, and Leonidas Bachas. Correction to can temperature be used to tune the selectivity of membrane ion-selective electrodes? *Analytical chemistry*, 83, 06 2011.

[66] Ashraf Islam. Design and optimization of printed circuit board inductors for wireless power transfer system. *Circuits and Systems*, 04:237–244, 01 2013.